# A novel somatosensory spatial navigation system outside the hippocampal formation

Xiaoyang Long and Sheng-Jia Zhang*

*Department of Neurosurgery, Xinqiao Hospital, Army Medical University, Chongqing, China*

*To whom correspondence should be addressed.

Correspondence and requests for materials should be addressed to:

sheng-jia.zhang@tmmu.edu.cn or sheng-jia.zhang@outlook.com

# Abstract

Spatially selective firing in the forms of place cells, grid cells, border cells and head direction cells are basic building blocks of a canonical spatial circuit centered on the hippocampal-entorhinal complex. While head direction cells can be found throughout the brain, spatial tuning outside of the parahippocampal regions are often non-specific or conjunctive to other representations such as a reward. While the precise mechanism of spatially selective activities is not understood, various studies show sensory inputs (particularly vision) heavily modulate spatial representation in the hippocampal-entorhinal circuit. To better understand the contribution from other sensory inputs in shaping spatial representation in the brain, we recorded from the hindlimb region of the primary somatosensory cortex (S1HL) in foraging rats. To our surprise, we were able to identify the full complement of spatial activity patterns reported in the hippocampal-entorhinal circuit, namely, place cells, head direction cells, boundary vector/border cells, grid cells and conjunctive cells. This novel finding supports the hypothesis that location information is necessary for body representation in the S1, and may be analogous to spatially tuned representations in the motor cortex relating to the movement of body parts. Our findings are transformative in our understanding of how spatial information is used and utilized in the brain, as well as functional operations of the S1 in the context of rehabilitation with brain-machine interfaces.

# Introduction

Spatial representation in the brain has been largely associated with the hippocampus and the entorhinal cortex (Buzsaki and Moser, 2013; Moser et al., 2017). Place cells (O'Keefe and Dostrovsky, 1971) were originally discovered in the hippocampus, with boundary vector/border cells (Lever et al., 2009; Solstad et al., 2008), grid cells (Hafting et al., 2005) and conjunctive cells (Sargolini et al., 2006) discovered later in the entorhinal cortex. Unlike the location-specific spatial cells in the hippocampal-entorhinal circuit, head direction cells (Ranck, 1985; Taube et al., 1990) can be found in areas ranging from the diencephalon to thalamic, striatal and cortical regions (Cullen and Taube, 2017).

Despite the focus on hippocampal-entorhinal contributions to spatial representation, location-dependent firing conjunctive to other sensory/cognitive (e.g. reward) information have been reported in sensory areas (Fiser et al., 2016; Ji and Wilson, 2006; Town et al., 2017) and cortical regions heavily interconnected with the hippocampal-entorhinal system such as the septum, subicular complex, parietal cortex and retrosplenial cortex (Alexander and Nitz, 2017; Boccara et al., 2010; Leutgeb and Mizumori, 2002; Rancz et al., 2015; Wilber et al., 2014). However, the only extra-parahippocampal region exhibiting apparent location-dependent firing restricted to space alone is the anterior claustrum, where stable, visually-anchored place cell- and border cell-like activities can be recorded (Jankowski and O'Mara, 2015). A preliminary report also suggests the dorsal geniculate nucleus may contain place cells similar to those found in the hippocampus (Hok et al., 2018). While there are place cell-like activities in the monkey sensorimotor cortices (Tseng et al., 2018; Yin et al., 2018), it is unclear if these spatial representations are comparable to their rodent equivalents.

The exact physiological mechanism of spatial selectivity in the hippocampal-entorhinal system is incompletely understood. Lesions to either area severely affect, but do not abolish spatially selective activities in the other (Bonnevie et al., 2013; Hales et al.,

2014). Past studies have shown manipulation of visual cues (Jezek et al., 2011; Muller and Kubie, 1987; Quirk et al., 1990), olfaction (Zhang and Manahan-Vaughan, 2013) and vibrissae inputs (Gener et al., 2013) all impact on hippocampal place cell activity, yet none are necessary. Recent theoretical work has suggested the somatosensory area may contain higher-order presentations of the body itself beyond elementary sensory information, of which location presentation is integral in a "body simulation" model of somatosensation (Brecht, 2017). Developmental studies also suggest early spatial-related activities are less dependent on visual inputs that become more salient through maturation, and that spatial representation may depend on the perception of self-motion (Bjerknes et al., 2018; Bjerknes et al., 2015). Based on the assumption that somatosensation should play a major role in sensory inputs shaping parahippocampal spatial activity (McNaughton et al., 2006; Poucet et al., 2015; Ravassard et al., 2013) and spatial presentation has been theorized to be crucial for body representation (Brecht, 2017), we sought to identify spatially selective activities in the hindlimb (HL) region of the primary somatosensory cortex (S1). Remarkably, we were able to detect all spatial cell types reported in the hippocampal-entorhinal system (Moser et al., 2008; Moser et al., 2017) within the S1. We show these spatial-related activities share similar properties to their parahippocampal counterparts in terms of stability and response to environmental manipulations (Long and Zhang, 2018).

# Results

## Extracellular recording from the S1HL

We obtained neurophysiological recordings in behaving rats by using tetrodes mounted on movable microdrives. We recorded 1385 putative single units from five rats across 157 sessions. Recordings were obtained from layers IV to VI within the S1HL area (**Fig. 1A**; **Fig. S1**), as confirmed by histological reconstruction. The tetrodes were generally lowered in steps of either 25 μm or 50 μm per day. The recording sessions lasted between 10 to 20 minutes to ensure sufficient coverage of the whole arena, which was facilitated by foraging food pellets intermittently thrown into the arena. Spike

sorting was performed manually offline using TINT (Axona, St. Albans, U.K.). The separation of the clusters and waveforms was quantitatively measured with an isolation distance and the L-ratio (Harris et al., 2001; Schmitzer-Torbert and Redish, 2004) (**Fig. S2**).

We applied the same analysis described in previous work (Solstad et al., 2008; Zhang et al., 2013) on 1385 S1HL cells and 252 met the criteria for various types (e.g. place, head direction, border and grid cells) of spatial tuning (**Fig. S1C**). The distribution of different spatial cell types suggested, at least between layers IV and VI, there was a tendency for head direction cells to avoid layer VI and the presence of spatially tuned S1HL cells was sparse in superficial layer V. Place cells appeared to predominate deeper layers (**Figs. S1D-E**).

## Place cells in the S1HL

As illustrated in **Fig.1**, S1HL cells possessing place cell-like properties were the most abundant spatial cell type encountered (**Fig. S1C**). Spatially selective firing patterns similar to those originally described for hippocampal place cells (O'Keefe and Dostrovsky, 1971) can be observed (**Fig. 1B)**. These S1HL place cells were classified if their spatial information (SI) score (Skaggs et al., 1996) exceeds a stringent 99$^{th}$ percentile threshold (SI > 1.74 cut-off) from individually and population-based distribution of shuffled rate maps (**Figs. 1C-D**). The within-cell shuffling gave similar results to the population shuffling, in consistent with the previous study (Tukker et al., 2015). 116 out of the 1385 S1HL neurons (8.4%) met criterion and thus are referred to as “place cells” from here on. The average SI in bits per spike of all 116 classified S1HL place cells was 2.40 ± 0.06 (mean ± s.e.m.). This percentage was significantly higher than expected by random selection from the entire shuffled population (**Fig. 1D**; $Z$ = 27.58, $P < 0.001$; binomial test with expected $P_0$ of 0.01 among large samples).

We noted that if a 95$^{th}$ percentile criterion was applied as in some previous studies (Langston et al., 2010; Rubin et al., 2014; Wills et al., 2010), 342 out of the 1385 S1HL

neurons (24.7%) would be classified as place cells (average SI of 1.67 ± 0.04; cut-off = .88). This percentage was substantially higher than expected with random selection from the entire shuffled population (**Fig. 1D**; $Z = 33.64$, $P < 0.001$; binomial test with expected $P_0$ of 0.01 among large samples). In comparison to previous reports in the hippocampus, there appeared to be a lower percentage of place cells in the S1HL (24.7%) compared to the hippocampus CA1 (15/24, (Langston et al., 2010)), but SI scores appeared to be higher (1.67 vs <1.2) in the S1HL. We also reported that average peak rate (S1HL: 8.72 ± 0.70 Hz vs hippocampus: 7.92 ± 0.56 Hz), mean firing rate (S1HL: 0.49 ± 0.04 Hz vs hippocampus: 0.64 ± 0.1 Hz), field size (**Fig. 1F**; S1HL: 733.31 ± 42.60 $cm^2$ vs hippocampus: 619 ± 116 $cm^2$), average spatial coherence (**Fig. 1G** ; S1HL: 0.61 ± 0.02 vs hippocampus: ~0.6), spatial sparsity (**Fig. 1H**; S1HL: 0.11 ± 0.01 vs hippocampus: 0.32 ± 0.02) and proportion of multi-field place cells (S1HL: 29.3% vs hippocampus: 22.2%) were all comparable to hippocampal place cells (Fyhn et al., 2004; Jung et al., 1994; Kjelstrup et al., 2008; McNaughton et al., 1983; Skaggs et al., 1996; Wills et al., 2010). Besides, S1HL place cells can be found at any position within the arena (**Fig. 1E**) as in the hippocampus (Rich et al., 2014).

Place cell activity was defined not only by its location-specific firing, but also by the stability of its spatial representation. We computed within-trial rate map correlations to be 0.55 ± 0.05 between the two halves of a recording session (**Fig. S3B**), which remain stable in extended recording sessions up to 30 min (**Fig. S4B**). This result was similar to the average spatial stability being about 0.45 for the rat hippocampal CA1 place cells (Langston et al., 2010). Hippocampal place cell activities were known to be heavily modulated by visual cues (Jezek et al., 2011; Muller and Kubie, 1987; Quirk et al., 1990), and were known to rotate with the positioning of visual cues (Muller and Kubie, 1987; O'Keefe and Conway, 1978). We performed similar experiments to test if S1HL place cell activities were modulated by visual cues by moving it 90° from its original position and back. Remarkably, the relative position of S1HL place fields did indeed rotate with the placement of the visual cue and remained stable after the cue was moved back to its original position (**Fig. S4A**).

To measure the animal's running speed within and outside the firing fields of S1HL place cells, we calculated the average "in-field" and "out-field" running speed (> 2.5 cm/s) for 116 identified place cells in S1HL. We quantified the average running speed across all the spatial bins within the firing field of the place cell ("in-field" running speed) as well as outside the firing field of the place cell ("out-field" running speed) (**Fig. S5A**). We found that there was no significant difference between the average "in-field" and "out-field" running speed (15.74 ± 0.22 cm/s vs 15.50 ± 0.31 cm/s, $n$ = 116, $P$ = 0.36, two-tailed paired $t$-test, **Fig. S5B**).

Theta rhythmicity and phase precession of hippocampal place cells and entorhinal grid cells play important roles for episodic memory and spatial navigation in the hippocampal-entorhinal network (Buzsaki and Moser, 2013; O'Keefe and Recce, 1993; Ray et al., 2014). Similar to hippocampal and entorhinal theta local field activities, we also observed prominent theta oscillations (4-11 Hz) (**Fig. S6A** and **Fig. S6C**) and significant theta power (**Fig. S6B** and **Fig. S6D**) in the S1HL during locomotion. Additionally, S1HL place cells were significantly theta-modulated and showed theta precession ($P$ < 0.001, 0.001 and 0.001, respectively, lower panels in **Fig. S7**).

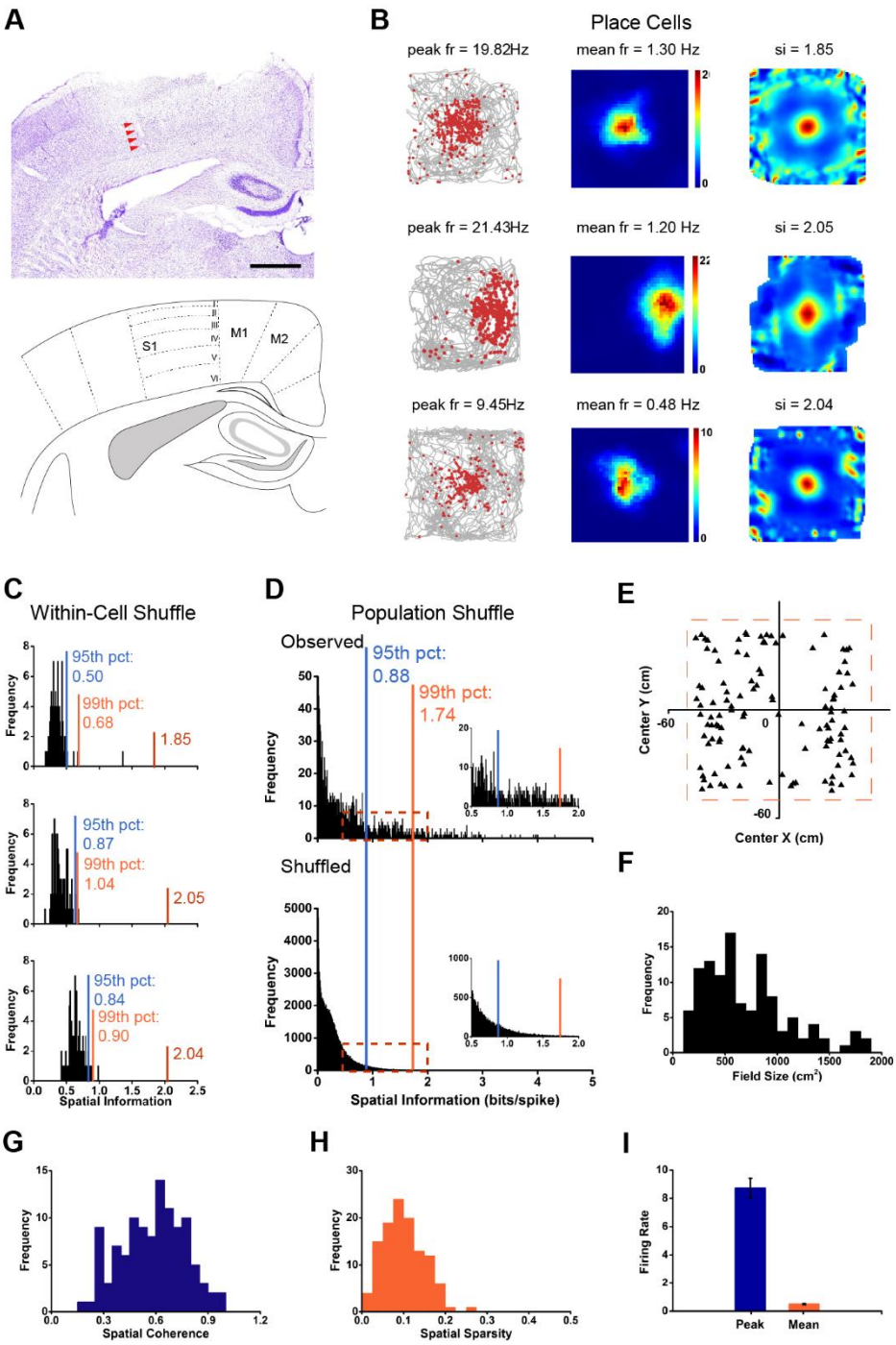


**Fig. 1 Place cells in the somatosensory cortex.**

**(A)** A Nissl-stained coronal section (upper) showing tetrode tracking trajectory (arrowheads) through all of six layers across the rat primary somatosensory cortex. The bottom panel shows the schematic delimitation of the different layers and sub-regions of the somatosensory cortex. Scale bar, 1 mm. (**B)** Trajectory (grey line) with superimposed spike locations (red dots) (left column); heat maps of spatial firing rate (middle column) and autocorrelation (right column) are color-coded with dark blue

indicating minimal firing rate and dark red indicating maximal firing rate. The scale of the autocorrelation maps is twice that of the spatial firing rate maps. Peak firing rate (fr), mean firing rate (fr) and spatial information (si) for each representative cell are labelled at the top of the panels. (**C)** Distribution of within-cell shuffled spatial information for three representative somatosensory place cells. The orange and blue stippled lines mark the 99$^{th}$ and the 95$^{th}$ percentile significance level of each randomly shuffled distribution, respectively. The red line indicates the observed spatial information. (**D)** Distribution of spatial information for all isolated somatosensory units. The top panel shows the distribution for observed spatial information. The bottom panel shows the distribution for randomly shuffled data from the same sample. The orange and blue stippled lines mark the 99$^{th}$ and the 95$^{th}$ percentile significance level of each randomly shuffled distribution, respectively. A zoomed panel shows the magnification of the specified area marked by the red dashed rectangle. (**E**) The areal distribution of various place firing fields relative to the field center. (**F-H**) The population histograms of place firing field sizes (**F**), spatial coherence (**G**) and spatial sparsity (**H**) for all of 116 identified somatosensory place cells. (**I**) The peak and mean firing rates (± s.e.m.) for all identified somatosensory place cells.

## Head direction cells in the S1HL

Head direction cells discharge only when the animal's head is at a particular angle respective to the environment (Ranck, 1985; Taube et al., 1990). To classify the preferred firing angle of each cell, the mean vector length was used to compute head direction tuning (Rubin et al., 2014; Sargolini et al., 2006). Cells were categorized as head direction cells if the mean vector length exceeded the 99$^{th}$ percentile of the total distribution of the shuffling procedure from the entire pool of putative single cells (**Fig. 2C**). 55 cells (3.97% of all recorded cells) met the criterion, showing significant modulation with the animal's head direction (**Fig. 2A**), with the average mean vector length found to be 0.56 ± 0.02. Besides, the within-cell shuffling for those three representative somatosensory head direction cells generated similar results to the population shuffling (**Fig. 2B**). This percentage is significantly higher than expected by

random selection from the entire shuffled population (**Fig. 2C**; $Z$ = 11.11, $P$ < 0.001; binomial test with expected $P_0$ of 0.01 among large samples). Notably, 185/1385 S1HL (13.36%) fulfilled the lower 95$^{th}$ percentile criterion with the average length of the mean vector found to be 0.38 ± 0.01.

Compared to previous reports in the subicular complex and the medial entorhinal cortex (MEC) (Boccara et al., 2010), the head direction tuning of S1HL cells appeared to be sharper, as measured by the average full width at half maximum (FWHM) of the angular distributions (36.05 ± 2.76 degrees for S1HL vs 53.0 ± 1.4 degrees for presubiculum, 67.4 ± 1.9 degrees for parasubiculum or 66.5 ± 2.3 degrees for MEC). The distribution of head direction preferences was uniformly distributed (Rayleigh test for uniformity: $P$ = 0.60, **Fig. S8**). We found head direction related firing to be stable within sessions, with the average angular correlation coefficient for S1HL head direction cells being 0.45 ± 0.03 (**Fig. S9**), similar to the median angular stability being around 0.5 for head direction cells in rat presubiculum (Tukker et al., 2015) and the average angular stability being about 0.55 for head direction cells in MEC (Langston et al., 2010; Wills et al., 2010). As with hippocampal place cells, head direction cells also anchored to salient visual cues (Goodridge et al., 1998). We further tested the specificity and stability of S1HL head direction cells by rotating a salient visual cue 90° from its original position in the enclosure and back (as in S1HL place cells described above). As with S1HL place cells, S1HL head direction cells also rotated with the movement of the salient visual cue (**Fig. S10**).

To measure the difference of the animal's angular velocity within and outside preferred firing directions for those identified head direction cells in S1HL, we calculated the average angular velocity in the "preferred firing directions" and "non-preferred firing directions" for 55 identified head direction cells in S1HL (**Fig. S11A**). We found that there was no significant difference between the average angular velocity in the "preferred firing directions" and "non-preferred firing directions" for head direction cells in S1HL (52.30 ± 1.96 degrees/s vs 55.92 ± 0.80 degrees/s, $n$ = 55, $P$ = 0.12, two-

tailed paired *t*-test, **Fig. S11B**).

Although the previous study had shown that food chasing had little effect on head directional firing in the rat anterior thalamic nuclei (Taube, 1995), we evaluated the firing patterns of head direction cells in the S1HL without food pellet dispersion. We recorded the same head direction cell in two consecutive secessions with (bottom panels in **Fig. S12A**) and without (upper panels in **Fig. S12A**) food pellets, respectively. No significant differences were observed to suggest food chasing modulated preferred firing angles in S1HL head direction cells. Similar results were observed for place cells in the S1HL without throwing food pellets within the running arena (**Fig. S12B**).

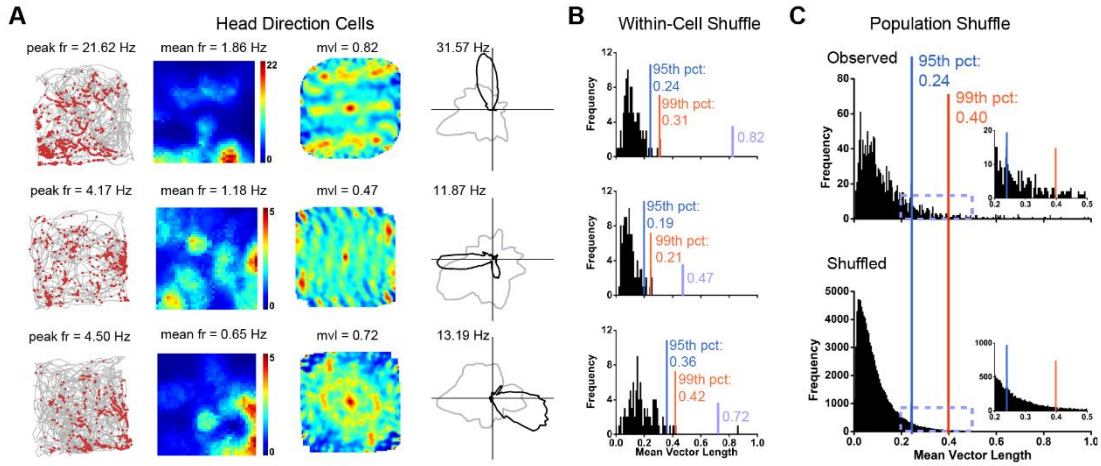


**Fig. 2 Head direction cells recorded from the somatosensory cortex.**

**(A)** Three examples of somatosensory head direction cells. Trajectory (grey line) with superimposed spike locations (red dots) (left column); spatial firing rate maps (middle left column), autocorrelation diagrams (middle right column) and head direction tuning curves (black) plotted against dwell-time polar plot (grey) (right column). Firing rate is color-coded with dark blue indicating minimal firing rate and dark red indicating maximal firing rate. The scale of the autocorrelation maps is twice that of the spatial firing rate maps. Peak firing rate (fr), mean firing rate (fr), mean vector length (mvl) and angular peak rate for each representative head direction cell are labelled at the top of the panels. The directional plots show strong head direction tuning. **(B)** Distribution of within-cell shuffled mean vector length for three representative somatosensory head

direction cells. The orange and blue stippled lines mark the 99th and the 95th percentile significance level of each randomly shuffled distribution, respectively. The purple line indicates the observed mean vector length. (**C**) Distribution of mean vector length for all identified somatosensory units. The top panel shows the distribution for observed values. The bottom panel shows the distribution for randomly shuffled data from the same sample. The orange and blue stippled lines mark the 99th and the 95th percentile significance level of each randomly shuffled distribution, respectively. A zoomed panel shows the magnification of the specified area marked by the purple dashed rectangle.

## Border coding in the S1HL

Border cells discharge exclusively whenever an animal is physically close to one or several environmental boundaries, for example, the enclosure walls of the recording arena (Lever et al., 2009; Solstad et al., 2008). S1HL cells were defined as border cells if border scores (see Methods) were larger than the 99th percentile of population shuffled scores (**Fig. 3C**). A total of 48/1385 (3.5%) S1HL cells were classified as border cells, and this percentage was significantly higher than expected by random selection from the entire shuffled population (**Fig. 3C**; $Z = 9.22$, $P < 0.001$; binomial test with expected $P_0$ of 0.01 among large samples). Similar results were observed by performing cell-specific shuffling for those three representative somatosensory border cells (**Fig. 3B**). Most border cells fired along a single boundary while others were active along with two, three or even four boundaries within the enclosure (**Fig. 3A**). The average firing rate and the border score were 0.69 ± 0.12 Hz and 0.57 ± 0.01, respectively. This was consistent with the average firing rate being 0.90 ± 0.12 Hz and border score being ~ 0.6 for border cells in the MEC (Bjerknes et al., 2014). At a lower 95th percentile criterion, 143/1385 (10.3%) S1HL cells were classified as border cells.

Qualitatively, S1HL border cells maintained their border-specific firing fields between circular and square enclosures (**Fig. S13A**), comparable to border cells from the presubiculum, parasubiculum and MEC (Boccara et al., 2010; Solstad et al., 2008). S1HL border cells also responded to a new wall insert to a familiar enclosure (**Fig.**

**S13B**), as described in the MEC (Solstad et al., 2008). As observed in the MEC, removal of walls from the enclosure on an elevated platform reversibly increased spiking in the center with preserved "border" specificity (Solstad et al., 2008), suggesting S1HL border cells, too, coded for geometric boundaries instead of physical borders (**Fig. S14**). Interestingly, we also detected a small number of boundary vector cells (Lever et al., 2009) which discharged further away from the edge of the enclosure (**Fig. S15**).

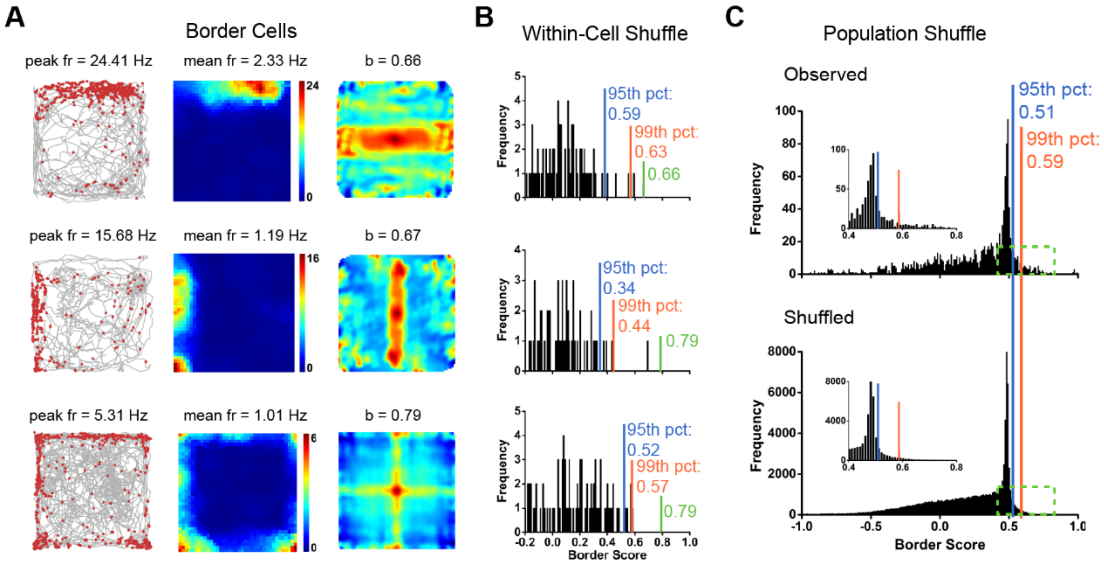


**Fig. 3 Border cells recorded from the somatosensory cortex.**

**(A)** Three representative examples of somatosensory border cells. Trajectory (grey line) with superimposed spike locations (red dots) (left column); heat maps of spatial firing rate (middle column) and autocorrelation diagrams (right column). Firing rate is color-coded with dark blue indicating minimal firing rate and dark red indicating maximal firing rate. The scale of the autocorrelation maps is twice that of the spatial firing rate maps. Peak firing rate (fr), mean firing rate (fr) and border score (b) for each representative border cell are labelled at the top of the panels. (**B**) Distribution of within-cell shuffled border score for three representative somatosensory border cells. The orange and blue stippled lines mark the 99$^{th}$ and the 95$^{th}$ percentile significance level of each randomly shuffled distribution, respectively. The green line indicates the observed border score. (**C**) Distribution of border scores for pooled somatosensory cells. The top panel shows the distribution for observed values. The bottom panel shows the

distribution for randomly shuffled versions from the same sample. The orange and blue stippled lines mark the 99th and the 95th percentile significance level of each randomly shuffled distribution, respectively. A zoomed panel shows the magnification of the specified area marked by the green dashed rectangle.

## Grid cells in the somatosensory cortex

Hexagonal firing patterns identified in the MEC (Hafting et al., 2005) can also be observed in the S1HL. To quantify the regularity of hexagonal firing patterns of the S1HL cells (**Fig. 4A**), we calculated grid scores based on rotated autocorrelograms of rate maps. A cell was categorized as a grid cell if its grid score was higher than the 99th percentile of the shuffled data. 56/1385 cells (4.0%) met this criterion (**Fig. 4C**), and this percentage was significantly higher than expected by random selection from the entire shuffled population (**Fig. 4C**; $Z = 11.92$, $P < 0.001$; binomial test with expected $P_0$ of 0.01 among large samples). Similar results were observed by performing within-cell shuffling (**Fig. 4B**). The average firing rate and the grid score were 1.46 ± 0.31 Hz and 0.55 ± 0.02, respectively. This was comparable to the average firing rate of 1.43 ± 0.13 Hz and the grid score of 0.60 ± 0.03 reported in the MEC (Buetfering et al., 2014).

Grid spacing in S1HL cells (**Fig. 4D**) was 41.30 ± 1.68 cm, compared to 39.1-43.0 cm from dorsal MEC grid cells (Hafting et al., 2005). The average grid size (782.69 ± 75.24 $cm^2$, **Fig. 4E**) was slightly larger than that from the dorsal (353-583 $cm^2$) or ventral (511-637 $cm^2$) MEC (Hafting et al., 2005). Moreover, the grid orientation (26.44 ± 2.44 degrees) in the S1HL (**Fig. 4F**) was similar to their MEC (19.7-32.7 degrees) counterparts(Hafting et al., 2005). Again, with a lower threshold at the 95th percentile, 189/1385 S1HL neurons (13.6%) were classified as grid cells, with the grid score threshold of 0.17 (blue line in **Fig. 4C**). In addition, we found most of the somatosensory grid cells were also theta-modulated and exhibited phase precession (**Figs. S16A-C**). Taken together, the local configuration of grid cells in the somatosensory cortex exhibited similar features as those in MEC. Strikingly, we detected irregular grid cells with negative grid scores in the S1HL along with regular

grid cells (**Fig. 4G**). Interestingly, irregular somatosensory grid cells were also theta-modulated and showed phase precession (**Figs. S16D-F**).

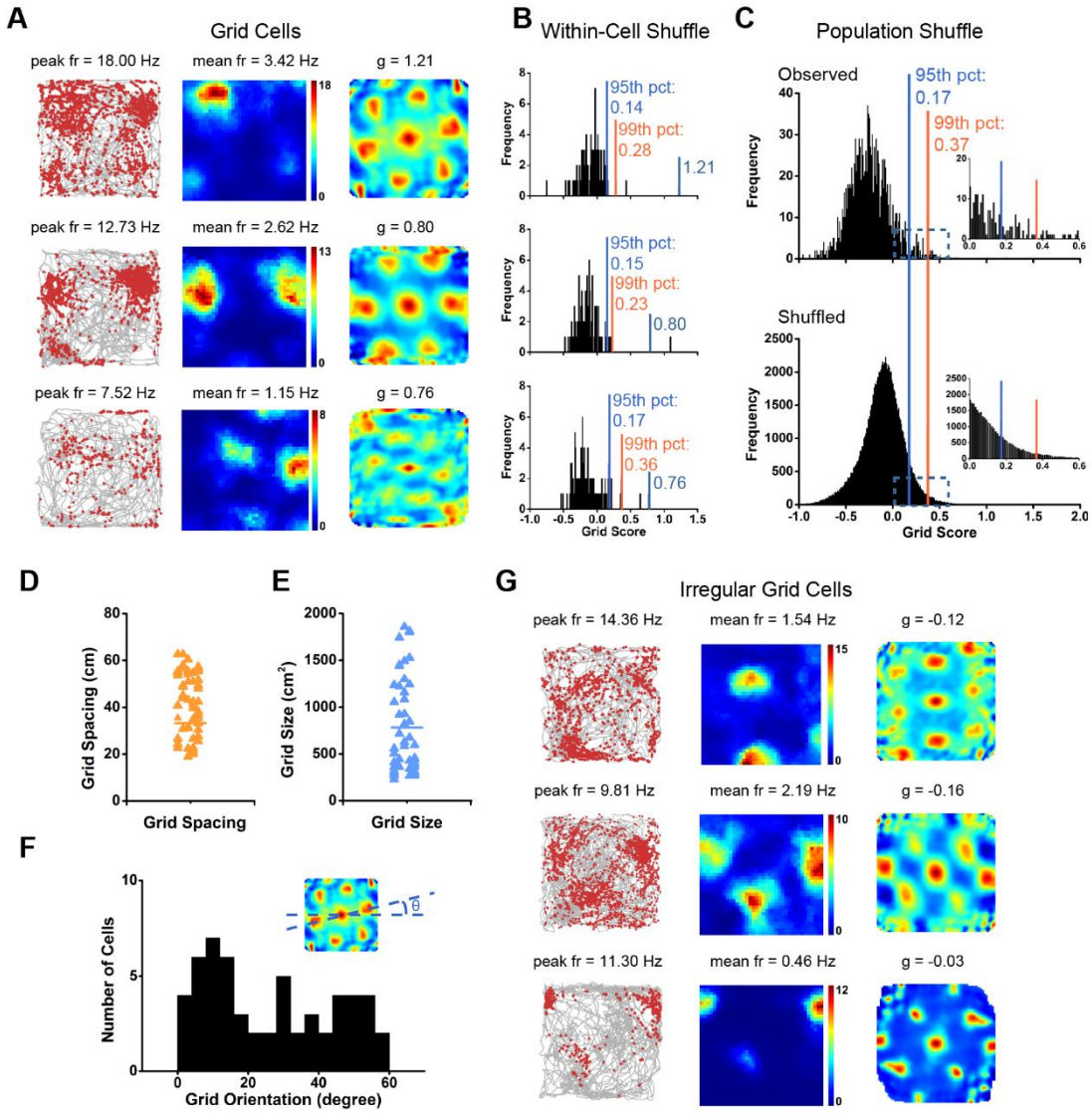


**Fig. 4 Grid cells in the somatosensory cortex.**

**(A)** Three representative examples of somatosensory grid cells. Trajectory (grey line) with superimposed spike locations (red dots) (left column); heat maps of spatial firing rate (middle column) and autocorrelation diagrams (right column). Firing rate is color-coded with dark blue indicating minimal firing rate and dark red indicating maximal firing rate. The scale of the autocorrelation maps is twice that of the spatial firing rate maps. Peak firing rate (fr), mean firing rate (fr) and grid score (g) for each representative grid cell are labelled at the top of the panels. A crystal-like hexagonal firing pattern was observed. **(B)** Distribution of within-cell shuffled grid score for three representative

somatosensory grid cells. The orange and blue stippled lines mark the 99$^{th}$ and the 95$^{th}$ percentile significance level of each randomly shuffled distribution, respectively. The cyan line indicates the observed grid score. (**C**) Distribution of grid scores for somatosensory cells. The top panel shows the distribution for observed values. The bottom panel shows the distribution for randomly shuffled versions from the same sample. The orange and blue stippled lines mark the 99$^{th}$ and the 95$^{th}$ percentile significance level of each randomly shuffled distribution, respectively. A zoomed panel shows the magnification of the specified area marked by the cyan dashed rectangle. (**D-E**) The raster plots show the distribution of grid spacing and grid size of the classified somatosensory grid cells. (**F**) The histogram of grid orientation from categorized somatosensory grid cells. (**G**) Three representative examples of irregular somatosensory grid cells.

## Conjunctive cells in the S1HL

To establish the existence of S1HL neurons coding more than one spatial correlate, we assessed the strength of head direction tuning for all S1HL place cells, border cells and grid cells (Rubin et al., 2014; Sargolini et al., 2006). A small number of S1HL neurons were found to be conjunctive cells (**Fig. 5**). Specifically, 19/116 place cells (**Fig. 5A**), 4/48 border cells (**Fig. 5B**) and 3/56 grid cells (**Fig. 5C**) were significantly tuned by head direction. Interestingly, we also detected irregular hexagonal grid cells modulated with head direction (**Fig. 5D**).

The degree of directionality in conjunctive cells showed no obvious difference from that of pure head direction cells (mean $U^2$ values, 11.88 and 13.81, respectively; $P > 0.05$). These results suggested that the somatosensory cortex carried similar conjunctive spatial x directional, border x directional and gird x directional signal to those identified previously in the rat subiculum (Cacucci et al., 2004), the rat MEC (Sargolini et al., 2006; Solstad et al., 2008) and Egyptian fruit bats (Yartsev et al., 2011).

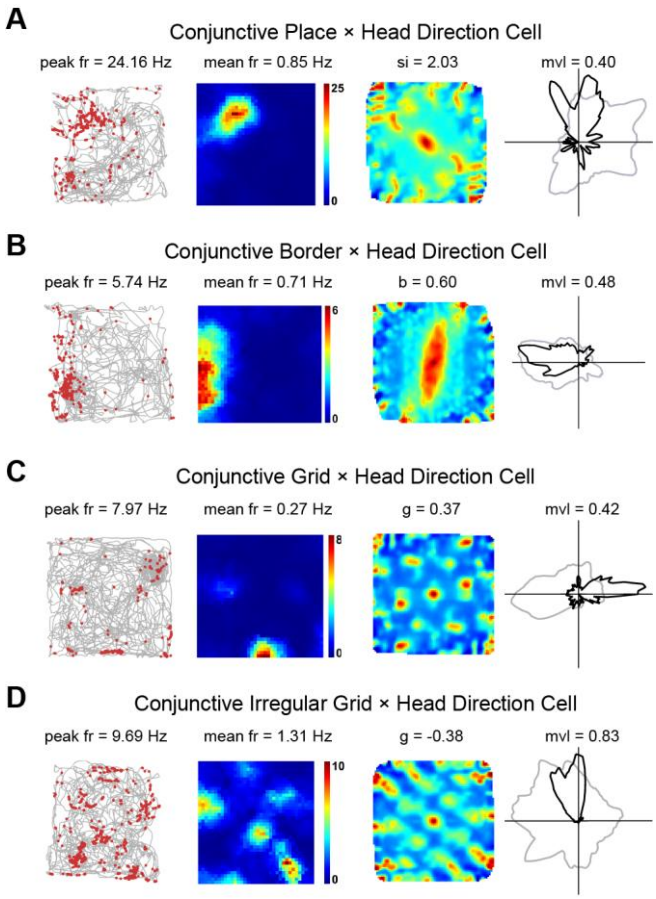


**Fig. 5 Four different types of conjunctive cells in the somatosensory cortex.** (**A**) A representative conjunctive place x head direction cell. (**B**) A representative conjunctive border x head direction cell. (**C**) A representative conjunctive grid x head direction cell. (**D**) A representative conjunctive irregular grid x head direction cell. Trajectory (grey line) with superimposed spike locations (red dots) (left column); heat maps of spatial firing rate (middle left column), autocorrelation diagrams (middle right column) and head direction tuning curves (black) plotted against dwell-time polar plot (grey) (right column). Firing rate is color-coded with dark blue indicating minimal firing rate and dark red indicating maximal firing rate. The scale of the autocorrelation maps is twice that of the spatial firing rate maps. Peak firing rate (fr), mean firing rate (fr), spatial information (si), border score (b), grid score (g) and mean vector length (mvl) for each representative cell are labelled at the top of the panels.

## Impact of the whisker trimming on the S1HL spatial activities

Since rodents use their whiskers to actively explore the external environment for

whisker-based navigation (Chorev et al., 2016; Sofroniew and Svoboda, 2015), we implanted two additional rats (**Fig. S1B**) and recorded neuronal activity before and after repeated whisker trimming (**Fig. S17A** and **Fig. S17C**) to gauge the involvement of the vibrissae. Two consecutive recording sessions from the same rat before and right after whisker trimming showed that the distribution of clusters and waveforms in the S1HL was qualitatively similar (**Fig. S17B** and **Fig. S17D**).

To further quantify the change of well-isolated spike clusters before and after whisker trimming, we calculated the isolation distance and L-ratio (Harris et al., 2001; Schmitzer-Torbert and Redish, 2004). The median isolation distances were 122.35 and 132.9 before and after whisker trimming, respectively. There was no significant difference in cluster separation and L-ratio in the S1HL before and right after whisker trimming (**Fig. S17E** and **Fig. S17F**, $n$ = 78, $P$ = 0.73 and 0.76, respectively, two-tailed paired $t$-test). The average drift of center of mass for the total cell sample before and after whisker trimming was 0.13 ± 0.01, indicating there was minimal change in spike clusters before and after whisker trimming. In addition, both peak and average firing rates of the same neurons before and after whisker trimming did not change significantly (**Fig. S17G** and **Fig. S17H**, $n$ = 78, $P$ = 0.75 and 0.47, respectively, two-tailed paired $t$-test).

To further assess whether whisker trimming affected the S1HL spatial firing properties, we were able to continuously record the same S1HL border cell before and after whisker trimming. The spatial firing patterns of the border cell persisted and responded to a new wall inserted into the square enclosure (**Fig. S18A** and **Fig. S18B**). Overall, both the spatial responses and firing properties in the S1HL were not significantly affected with the whisker trimming.

When we pooled and analyzed a total of 461 cells recorded after whisker trimming, we were still able to identify all different spatial cell types including 43 place cells (**Fig. 6A**), 15 head direction cells (**Fig. 6B**), 29 border cells (**Fig. 6C**) and 17 grid cells (**Fig. 6D**). The percentage of all recorded spatially tuned cell types after whisker trimming

were similar to those recorded from rats without whisker trimming. Furthermore, the cutoffs for defining place cells (**Fig. 6E**), head direction cells (**Fig. 6F**), border cells (**Fig. 6G**) and grid cells (**Fig. 6H**) after whisker trimming highly resembled those for different somatosensory spatial cell types without whisker trimming. Taken together, the persistence of recorded S1HL spatial cells after whisker trimming demonstrated that our identified cells were not significantly influenced by the whisker trimming.

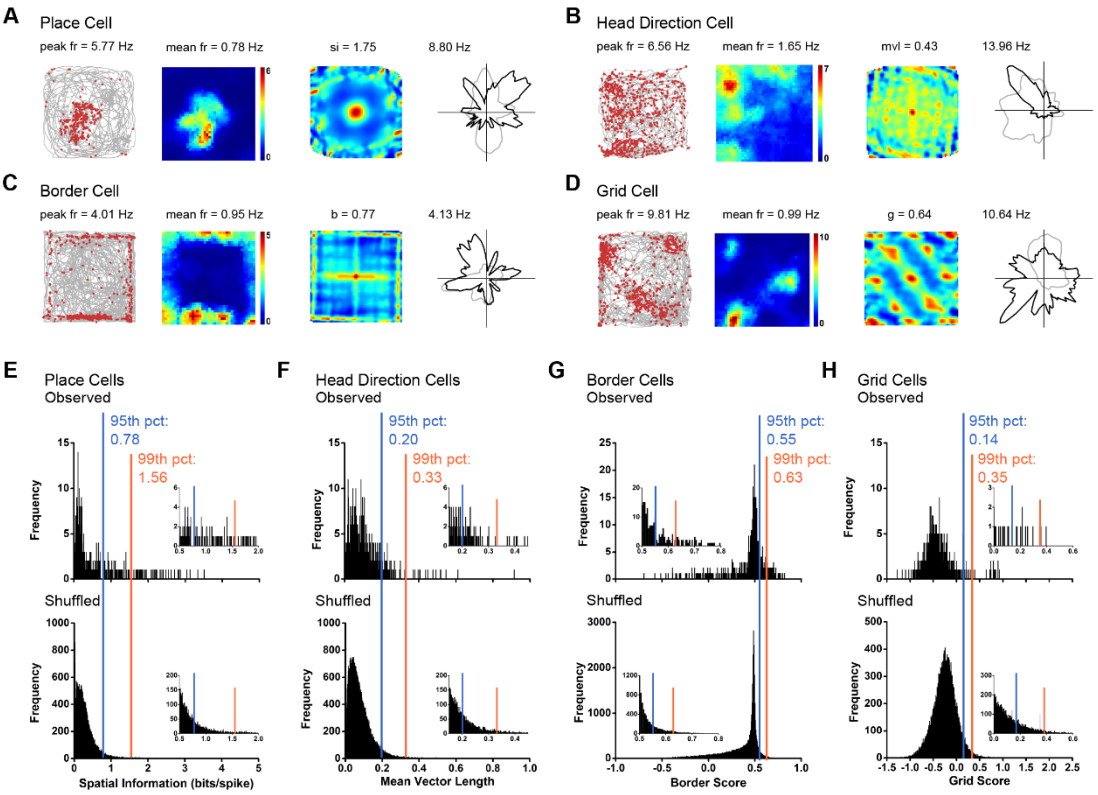


**Fig. 6 Somatosensory spatial response after the whisker trimming.**

**(A-D)** Four representative examples of somatosensory place cell (**A**), head direction cell (**B**), border cell (**C**) and grid cell (**D**) after whisker trimming. Trajectory (grey line) with superimposed spike locations (red dots) (left column); spatial firing rate maps (middle left column), autocorrelation diagrams (middle right column) and head direction tuning curves (black) plotted against dwell-time polar plot (grey) (right column). Firing rate is color-coded with dark blue indicating minimal firing rate and dark red indicating maximal firing rate. The scale of the autocorrelation maps is twice that of the spatial firing rate maps. Peak firing rate (fr), mean firing rate (fr), spatial information (si), mean vector length (mvl), border score (b) or grid score (g) and

angular peak rate for each representative cell are labelled at the top of the panels. (**E-H)** Distribution of spatial information (**E**), mean vector length (**F**), border score (**G**) or grid score (**H**) for somatosensory cells after whisker trimming. The top panel shows the distribution for observed values. The bottom panel shows the distribution for randomly shuffled data from the same sample. The orange and blue stippled lines mark the 99$^{th}$ and the 95$^{th}$ percentile significance level of each randomly shuffled distribution, respectively.

# Discussion

This study provides the first demonstration and characterization of spatially tuned neuronal discharges in the rat primary somatosensory cortex. We have shown place, grid, border, head direction and conjunctive cell activities, as reported in parahippocampal and associated areas (Moser et al., 2017), to co-exist in the primary somatosensory cortex. These spatially tuned activities appear to be specific, stable, anchored to external visual cues and robust against non-spatial environmental perturbations.

Based on the assumption that proprioception makes a significant contribution to spatial representation in the parahippocampal cortices (McNaughton et al., 2006; Poucet et al., 2015; Ravassard et al., 2013), we predicted spatially selective activities should exist in the S1. To our surprise, we were able to record the full complement of spatially selective cells (place, grid, border, head direction and conjunctive cells) in the HL region of S1. Given the paucity of direct projections from the parahippocampal areas to the S1HL region (Cenquizca and Swanson, 2007; Insausti et al., 1997), we assume S1HL spatial activities do not arise from the hippocampal-entorhinal circuit. However, we cannot completely eliminate the possibility that S1HL spatial activities may be at least partially dependent on the hippocampal-entorhinal system. Since there is very little overlap between septal projections to the hippocampal-entorhinal areas (Gaykema et al., 1990), and that septal inactivation severely attenuates place and grid cell activities in both regions (Bolding et al., 2019; Brandon et al., 2011; Koenig et al., 2011), how S1HL

responds to septal inactivation may provide the necessary insight for hippocampal-entorhinal dependency.

The laminar organization of the S1 in relation to connectivity and function has been well-characterized, largely arising from studies on the vibrissae barrel fields (Feldman and Brecht, 2005; Petersen, 2019). There is insufficient information on the specific connectivity patterns of S1HL in the rat, but mouse data suggest similar cortico-cortical, thalamic-cortical, cortical-thalamic, cortico-striatal and corticofugal connection patterns between S1HL and other parts of the S1 (Killackey and Sherman, 2003). Our current study is roughly limited to sampling layers IV through VI. There is a pattern for head direction cells to be absent in layer VI and place cells to predominate in deeper layers. From such distribution of spatial cell types across cortical depth, we could infer that head direction information is not present in cortico-thalamic communications, given the lack of head direction cells at depths corresponding to layer VI in S1HL. There also appears to be a gap in the most superficial aspect of layer V (Va) where all spatial cell types appear to be under-represented. Interestingly, layer Va projections are mostly recurrent (Yamawaki and Shepherd, 2015) and appear to serve as a trans-columnar and trans-laminar integration hub within the S1 (Larkum, 2013; Lefort et al., 2009; Schubert et al., 2001). Layer Va may serve as an area that integrates spatial and proprioceptive information in the S1, hence salient spatial activity is not readily observable in this layer. If true, this would also suggest that the major extra-cortical output from S1 combines, but do not contain conventional spatial information as characterized here. A full sampling of cortical layers in S1 using high-density linear probes (Buzsaki et al., 2015) is necessary to address how spatial information is generated, integrated and distributed elsewhere (e.g. thalamic, striatal and brainstem targets) in the brain.

As mentioned above, there is a lack of direct connections between S1HL and areas that are traditionally associated with spatial processing. Where do the spatial signals come from? Are they more universal in cortical processing than previously thought? What is

the functional significance of spatial activities in the S1HL, or S1 in general? While extensive intra and inter columnar/laminar exist in the S1 and may support *de novo* generation of place cells (from integrating local grid cell activities) and conjunctive cells, it is unlikely the full complement of known spatial representations are generated independently within the S1. We have demonstrated that S1HL place fields and preferred head direction rotate with the varied positioning of salient visual cue as cells found in the hippocampal-entorhinal circuit. This observation suggests the spatial activities cannot solely be driven by proprioception arising from lemniscal/paralemniscal pathways. While a sparse, direct and functional connection exist between the S1 and the visual cortex (Sieben et al., 2013), it is unlikely to account for visually anchored spatial tuning in the S1HL. Instead, S1HL spatial activities are more likely to be an efference copy from elsewhere in the brain.

S1 function and activities are intricately linked to motor structures, especially the motor cortex. Functional coupling between S1 spindle activity and spontaneous muscle twitches can be observed as early as two days after birth (Khazipov et al., 2004). It is known that both primary and secondary motor cortex are reciprocally connected with S1 (Akers and Killackey, 1978; Kaas, 1983; Welker and Sinha, 1972; Welker et al., 1988), and the preparation, execution and dynamic changes in movements can all be predicted from M1/S1 activities (Umeda et al., 2019). In fact, S1 has recently been shown to have an active role in directly controlling motor output (Karadimas et al., 2019). Position-dependent neuronal discharges (i.e. place field-like representations) relating to hand movement through space is well-established in the primate motor cortex (Ashe and Georgopoulos, 1994; Georgopoulos et al., 1984; Kettner et al., 1988; Paninski et al., 2004; Stark et al., 2009). In fact, considering movement of the hand or forelimb in general: speed (Ashe and Georgopoulos, 1994; Moran and Schwartz, 1999), (hand) direction (Ashe and Georgopoulos, 1994; Fu et al., 1995; Georgopoulos et al., 1982) and conjunctive (Ashe and Georgopoulos, 1994; Moran and Schwartz, 1999) coding in the motor cortices can be seen as homologous to their spatial navigation counterparts in the limbic system. Essentially, it appears the motor cortex contains

spatially tuned activities for specific body parts that are analogous to limbic activities that appear to represent whole body/head movement. Therefore, whole body/head and limb movements through space may require similar neurocomputation, of which is also present in the S1 in addition to motor and limbic cortices. This proposal is also consistent with the idea that S1 simulates the body itself in addition to its representation, which requires spatial information (Brecht, 2017). From this synthesis, we speculate that we would be able to record spatially tuned activities in the HL region of the motor cortex, as well as other sensorimotor cortices (e.g. the forelimb and trunk regions). Particularly, inactivation of the reciprocally connected motor cortex (i.e. HL region of the motor cortex) can test if S1HL spatial activities are efference copy from the motor cortex. Recent reports of place cell-like activities in the primate sensorimotor cortices (Tseng et al., 2018; Yin et al., 2018) during quasi-active movements through space support the notion that spatial representation of body movement may exist throughout the cortex.

Our discussion so far favors S1 spatial activity may be an efferent copy from the motor cortex. If true, then the question remains as to how an area such as the motor cortex without direct connectivity with spatially tuned limbic structures (like the S1) can acquire spatial activities. To the best of our knowledge, no grid- or border-like spatial representation has been reported in the motor cortex in conventional reaching studies, although this discrepancy may be related to that motor tasks in such studies are often limited to a single defined trajectory (insufficient spatial coverage to detect grid cells) in open task space (without physical borders). Likewise, the “body simulation” model (Brecht, 2017) predicts the existence of body part location information (which we interpret to be place cell-like representations) to exist in layer IV, but our data indicate the full complement of spatial activities can be detected from at least layers IV through VI. Our data is not fully compatible with currently available experimental and theoretical work in explaining why all currently recognized spatial cell activities can be found in S1 and how they are generated. Regardless, we propose it is likely spatial information is integral to the “body simulation” function in S1 as put forward by Brecht

(2017). High-resolution kinematic studies (Mathis et al., 2018) of body part (e.g. hindlimb) movements through space would be required to test if spatial activities in the S1 do in fact represent body parts in space.

In this report, we have demonstrated place, grid, border, head direction and conjunctive cell activities in the primary somatosensory cortex. These activities are comparable to their counterparts in the parahippocampal cortices and are stable, specific, robust to non-spatial manipulations and anchored to salient spatial cues. We propose spatial tuning in the primary somatosensory cortex may be crucial for body representation/simulation in space, and these spatial representations may generalize to other sensorimotor cortices pertinent to behavioral coordination.

# Materials and Methods

## Subjects

Seven male Long-Evans rats (2-4 months old, 250-450 grams at the time of the surgery) were used for this study. All animals were singly housed in transparent cages (35 cm x 45 cm x 45 cm, W x L x H) and maintained on a 12-hour reversed light-dark cycle (lights on at 9 p.m. and off at 9 a.m.). Experiments were performed during the dark phase. Rats were maintained in a vivarium with controlled temperature (19-22°C), humidity (55-65%). and were kept at about 85-90% of free-feeding body weight. Food restriction was imposed 8-24 hours before each training and recording trial. Water was available *ad libitum*. All animal experiments were performed in accordance with the National Animal Welfare Act under a protocol approved by the Animal Care and Use Committee from both Army Medical University and Xinqiao Hospital.

## Surgery and tetrode placement

Rats were anesthetized with isoflurane. Microdrives loaded with four tetrodes were implanted to target the hindlimb regions of the S1 (anterior-posterior (AP): 0.2-2.2 mm posterior to bregma; medial-lateral (ML): 2.2-3.4 mm lateral to midline, dorsal-ventral (DV): 0.4/0.6-3 mm below the dura.), secured with dental cement with 8-10 anchor

screws. A screw served as the ground electrode. Tetrodes were assembled with four 17 µm Platinum/Iridium wires (#100167, California Fine Wire Company). Tetrodes had impedances between 150 and 300 kΩ at 1 kHz through electroplating (nanoZ; White Matter LLC). 8-10 jeweler screws were attached into the rat skull, and individual microdrives were anchored to screws with several rounds of application of the dental cement.

## Training and data collection

Behavioral training, tetrode turning and data recording started one-week post-surgery. Rats were trained to run around in a 1 m x 1 m square box with a white cue card (297 mm x 210 mm) mounted on one side of the wall. Food pellets were scattered into the arena intermittently to encourage exploration.

Each recording session lasted between 10 and 20 min to facilitate full coverage of the testing arena. Tetrodes were lowered in steps of 25 or 50 µm daily until well-separated single units can be identified. Data were acquired by an Axona system (Axona Ltd., St. Albans, U.K.) at 48 kHz, band-passed between .8-6.7 kHz and a gain of x5-18k. Spikes were digitized with 50 8-bit sample windows. Local field potentials were recorded from one of the electrodes with a low-pass filter (500 Hz).

## Spike sorting, cell classification and rate map

Spike sorting was manually performed offline with TINT (Axona Ltd, St. Albans, U.K.), and the clustering was primarily based on features of the spike waveform (peak-to-trough amplitude and spike width), together with additional autocorrelations and cross-correlations (Skaggs et al., 1996; Wilson and McNaughton, 1993). During our manual cluster cutting, we always counted neurons with similar or identical waveform shapes only once whenever similar or identical individual neurons were recorded and tracked across two consecutive recording sessions. To confirm the quality of cluster separation, we calculated L-ratio as well as isolation distance between clusters.

Two small light-emitting diodes (LEDs) were mounted to the headstage to track the rats' speed, position and orientation via an overhead video camera. Only spikes with

instantaneous running speeds > 2.5 cm/s were chosen for further analysis in order to exclude confounding behaviors such as immobility, grooming and rearing.

To classify firing fields and firing rate distributions, the position data were divided into 2.5-cm x 2.5-cm bins, and the path was smoothed with a 21-sample boxcar window filter (400 ms; 10 samples on each side) (Boccara et al., 2010; Zhang et al., 2013). Cells with > 100 spikes per session and with a coverage of >80% were included for further analyses. Maps for spike numbers and spike times were smoothed with a quasi-Gaussian kernel over the neighboring 5 x 5 bins (Boccara et al., 2010; Langston et al., 2010; Zhang et al., 2013). Spatial firing rates were calculated by dividing the smoothed map of spike numbers with spike times. The peak firing rate was defined as the highest rate in the corresponding bin in the spatial firing rate map. Mean firing rates were calculated from whole session data.

## Analysis of place cells

Spatial information is a quantification of the extent to which a neuron's firing pattern can predict the position of freely moving animals and is expressed in the unit of bits per spike. The spatial information was calculated as:

$$\text{spatial information} = \sum_i p_i \frac{\lambda_i}{\lambda} \log_2 \frac{\lambda_i}{\lambda}$$

where $\lambda_i$ is the mean firing rate of the cell in the *i*-th bin, $\lambda$ is the overall mean firing rate of the cell in the trial, and $p_i$ is the probability for the animal being at the location of the *i*-th bin.

Adaptive smoothing (Skaggs et al., 1996) was applied to optimize the trade-off between spatial resolution and sampling error before the calculation of spatial information. The data were first divided into 2.5-cm x 2.5-cm bins, and then the firing rate within each bin was calculated by expanding a circle centered on the bin until

$$\gamma \geq \frac{\alpha}{n\sqrt{s}}$$

where $\gamma$ is the circle's radius in bins, $n$ is the number of occupancy of samples within the circle, $s$ is the total number of spikes fired within the circle, and $\alpha$ is a constant parameter set to 10,000. With a position sampling frequency at 50 Hz, the firing rate assigned to that bin was then set to $50 \cdot s/n$.

A place cell was classified as a cell with the spatial information above chance level, which was computed by a random permutation process using all recorded cells. For each round of the shuffling process, the entire sequence of spike trains from each cell was time-shifted along the animal's trajectory by a random period between 20 s and the trial duration minus 20 s, with the end wrapped to the beginning of the trial. A spatial firing rate map was then constructed, and spatial information was calculated. This shuffling process was repeated 100 times for each cell, generating a total of 138,500 permutations for the 1385 somatosensory neurons. This shuffling procedure preserved the temporal firing characteristics in the unshuffled data while disrupting the spatial structure at the same time.

Spatial information score was then measured for each shuffled rate map. The distribution of spatial information values across all 100 permutations of all cells was computed and finally, the 99$^{th}$ percentile of the significant level was determined. The threshold values for categorizing cells into place cells were defined as the spatial information scores above the 99$^{th}$ percentile of the distribution from shuffled populations. In addition to the population shuffling, the within-cell shuffling was also performed within the entire sequence of spike trains from each individual neuron, and the shuffling process was also repeated 100 times for each single cell.

Spatial sparsity was used to measure how compact and selective the place field of each place cell is relative to the recording enclosure. The spatial sparsity was calculated using the formula as follows (Skaggs et al., 1996):

$$\text{Sparsity} = \frac{(\sum p_i \lambda_i)^2}{\sum p_i {\lambda_i}^2}$$

Where $p_i$ is the occupancy probability for the animal being at the location of the $i$-th bin in the map and $\lambda_i$ is the mean firing rate of the cell in bin $i$.

Spatial coherence was estimated by calculating the mean correlation between the firing rate of each bin in the map and the aggregate firing rate of the eight nearest bins (Muller and Kubie, 1987). We used unsmoothed firing rate maps for computing the spatial coherence.

The spatial correlation across trials from the same recording arena was computed for each cell by correlating the firing rates in corresponding paired bins of two smoothed rate maps. The spatial stability within trials was estimated by calculating spatial (2D) correlations between firing rate maps generated from the first and second halves of the same trial.

## Analysis of grid cells

Spatial autocorrelation was calculated with smoothed rate maps (Boccara et al., 2010; Sargolini et al., 2006; Zhang et al., 2013). Autocorrelograms were derived from Pearson's product-moment correlation coefficient correcting for edge effects and unvisited locations.

With $\lambda(x, y)$ representing the average firing rate of a cell at coordinate $(x, y)$, the autocorrelation between the spatial firing field itself and the spatial firing field with lags of $\tau_x$ and $\tau_y$ was calculated as:

$$\mathrm{r}(\tau_x, \tau_y) = \frac{\mathrm{n} \sum \lambda(x,y)\, \lambda(x-\tau_x, y-\tau_y) - \sum \lambda(x,y) \sum \lambda(x-\tau_x, y-\tau_y)}{\sqrt{n \sum \lambda(x,y)^2 - [\sum \lambda(x,y)]^2} \sqrt{n \sum \lambda(x-\tau_x, y-\tau_y)^2 - [\sum \lambda(x-\tau_x, y-\tau_y)]^2}}$$

where the summation is over whole n pixels in $\lambda(x, y)$ for which firing rate was

calculated for both $\lambda(x, y)$ and $\lambda(x - \tau_x, y - \tau_y)$. Autocorrelations were not calculated for spatial lags of $\tau_x$, $\tau_y$ where $n < 20$.

The degree of spatial regularity ("gridness" or "grid score") was calculated for each unit by using a circular sample centered on the central peak of the autocorrelogram but excluding the central peak itself, and by comparing rotated versions of this circular sample (Sargolini et al., 2006; Solstad et al., 2008). The Pearson's correlations between this circular sample and its rotated versions were calculated, with the angles of rotation of 60° and 120° in the first group, and 30°, 90° and 150° in the second group. Gridness or the neuron's grid score was defined as the minimal difference between any of the coefficients in the first group and any of the coefficients in the second group. Shuffling was performed in the same procedure used for defining place cells. Grid cells were categorized as cells with the rotational symmetry-based grid scores exceeding the 99$^{th}$ percentile of the distribution of grid scores for shuffled data from the entire population of S1 cells.

Grid spacing was computed as the median distance from the grid center to the closest peak among six neighboring firing fields in the autocorrelogram of the spatial firing map. Since such analysis is sensitive to noise in the grid autocorrelogram, grid spacing was computed only when the median distance to the six neighboring peaks for the analyzed cell was comparable to the radius of the circle centered on the gird autocorrelogram with the highest grid score. The radius of this circle around the center of the autocorrelogram was also referred to as the grid field size.

Grid orientation was calculated by first computing vectors from the center of the autocorrelogram to each of the three adjacent peaks among six neighboring firing fields in the autocorrelogram of the spatial firing map in the counterclockwise direction, beginning with a camera-based reference line of zero degree. The angle between the minimal orientation of those three vectors and the camera-based reference line was defined as the grid orientation.

## Analysis of head direction cells

The rat's head direction was estimated by relative position of the LEDs differentiated through their sizes (Boccara et al., 2010; Langston et al., 2010; Sargolini et al., 2006; Zhang et al., 2013). The directional tuning curve for each recorded cell was drawn by plotting the firing rate as a function of the rat's head angle, which is divided into bins of 3 degrees and then smoothed with a 14.5-degree mean window filter (2 bins on each side). To avoid bias, data were only used if all head angle bins contain data.

The strength of directionality was calculated by computing the mean vector length from circular distributed firing rates. The chance values were determined by a shuffling process simulated in the same way as for place cells, with the entire sequence of spike trains time-shifted between 20 s and the whole trail length minus 20 s along the animal's trajectory. Cells were defined as head direction cells if the mean vector lengths of the recorded cells were larger than the $99^{th}$ percentile of the mean vector lengths in the shuffled distribution.

## Analysis of border cells

Border or boundary vector cells were identified by calculating, for each recorded cell, the difference between the maximal length of any of the four walls touching on any single spatial firing field of the cell and the average distance of the firing field to the nearest wall, divided by the sum of those two values (Boccara et al., 2010; Solstad et al., 2008; Zhang et al., 2013). Border scores ranged from −1 for cells with perfect central firing fields to +1 for cells with firing fields that exactly line up with at least one entire wall. Firing fields were defined as summation of neighboring pixels with total firing rates higher than 0.3 times the cell's maximum firing rate that covered a total area of at least 200 $cm^2$.

Border cell classification was verified in the same way as for place cells, head direction cells and grid cells. For each permutation trial, the whole sequence of spike trains was time-shifted along the animal's trajectory by a random period between 20 s and 20 s less than the length of the entire trial, with the end wrapped to the start of the trial. A

spatial firing rate map was then obtained, and a border score was estimated.

The distribution of border scores was calculated for the entire set of permutation trials from all recorded cells, and the 99$^{th}$ percentile was then determined. Cells were defined as border cells if the border score from the observed data was higher than the 99$^{th}$ percentile for border scores in the entire distribution generated from the permutated data.

## Analysis of theta modulation, phase precession and power spectral density

To calculate fluctuations of neural activity through the theta cycle, we offline-filtered local electroencephalography (EEG) signals according to the approach taken previously (Langston et al., 2010). For the low-pass filtering, 4 and 5 Hz were selected as stopband and passband low cut-off frequencies, respectively, while 10 and 11 Hz were selected as passband and stopband high cut-off frequencies, respectively. Every spike from single-unit waveform clusters was assigned a phase in relation to the filtered theta signal, with 0 degree and 180 degree defined as the peak and the trough of the filtered signal, respectively. The clustering of firing phases within the entire theta cycle was calculated with Rayleigh's test to evaluate the uniformity of circular distributions. The cell's degree of phase precession was fitted with a linear regression line, the significance of the phase precession was estimated with the *F*-test. Theta modulation of single-unit waveform clusters was calculated from the fast Fourier transform (FFT)-based power spectrum of the spike-train autocorrelation. When the mean spectral power within 1 Hz range of the theta peak within the 4-11 Hz frequency range was at least 3 times larger than the mean spectral power from 0 Hz to 125 Hz, the cell was defined as theta modulated. To quantify the theta rhythmicity of the local field potentials (LFP) within the somatosensory cortex, the LFP was bandpass-filtered with the theta range (4-11 Hz) to acquire theta-filtered LFP traces. Power spectral density was computed with FFT.

## Whisker trimming

To test how the removal of another salient somatosensation mediate by vibrissae input

impacts on FL/HL S1 spatial cells, we carefully trimmed all whiskers of each recoded rat bilaterally using blunt surgical scissors to within 1-2 mm above the skin surface just right before each recording session every day. Since bilateral whisker-trimmed rats did not exhibit abnormal behaviors, we continuously recorded somatosensory units from 2 whiskers-trimmed rats.

## Environmental manipulations

For visual landmark rotation, we first recorded neuronal activity in the standard session followed by 90° cue-card rotation in the clockwise or counterclockwise direction. Then another standard session was performed with the cue-card rotated back to the original position. For recording in the elevated platform without walls, we first recorded the S1HL spatial cells in the square box, followed by the recording in the elevated platform without walls. Finally, the animals were returned to the original square box for another recording session. For the recording of border cells in the presence of inserted wall, we first identified the S1HL border cells in the square box. Then the recording session was followed by the insertion of a wall along the center of the external wall. Another recording session was performed after removing the inserted wall. For food/no food comparisons, we recorded the S1HL spatial cells in two consecutive recording sessions without and with throwing food pellets into the running enclosure.

## Histology and reconstruction of recording positions

At the end of the experiment, rats were euthanized with an overdose of sodium pentobarbital and perfused transcardially with phosphate-buffered saline (PBS) followed by 4% paraformaldehyde (PFA). Brains were removed and stored in 4% PFA overnight. The brain was then placed in 10, 20 and 30% sucrose/PFA solution sequentially across 72 hours before sectioning using a cyrotome. Thirty micron sections were obtained through the implant region. Sections were mounted on glass slides and stained with cresyl violet (Sigma-Aldrich). The final recording positions were determined from digitized images of the Nissl-stained sections. Positions of each individual recordings were estimated from the deepest tetrode track, notes on tetrode advancement with tissue shrinkage correction by dividing the distance between the

brain surface and electrode tips by the last advanced depth of the recording electrodes. . All electrode traces were confirmed to be located within the S1defined by The Rat Brain Atlas (Paxinos and Watson, 2007).

**Acknowledgments**: We are indebted to H. Wu, W. Tang, Q. Ren, C. Zhang, H. Chen, S. Lv, H. Yang and J. Ni for their encouragement and generous help. We warmly thank J. Cai, B. Deng, S. Wang and L. Hu for their excellent technical assistance. We are grateful for the generous startup funds from Xinqiao Hospital (Grant# 2017A034) and Army Medical University (Grant# 2017R028), China. This work was supported by the National Natural Science Foundation of China through the Project Grant NSFC-31872775 to S.-J. Z. Original results published in this manuscript were previously uploaded on the preprint server for biology (https://www.biorxiv.org/content/10.1101/473090v1) at *bioRxiv* on November 19, 2018 (Long and Zhang, 2018).

**Author Contributions:** S.-J.Z. conceived and designed the study. X.L. and S.-J.Z. performed the experiments, collected the data and performed the analyses. X.L. made the figures. S.-J.Z. wrote the manuscript.

**Competing interests:** The authors declare no competing financial interests.

**Availability of Data and Materials:** All data and materials are available by reasonable request and should be directed to the corresponding author.

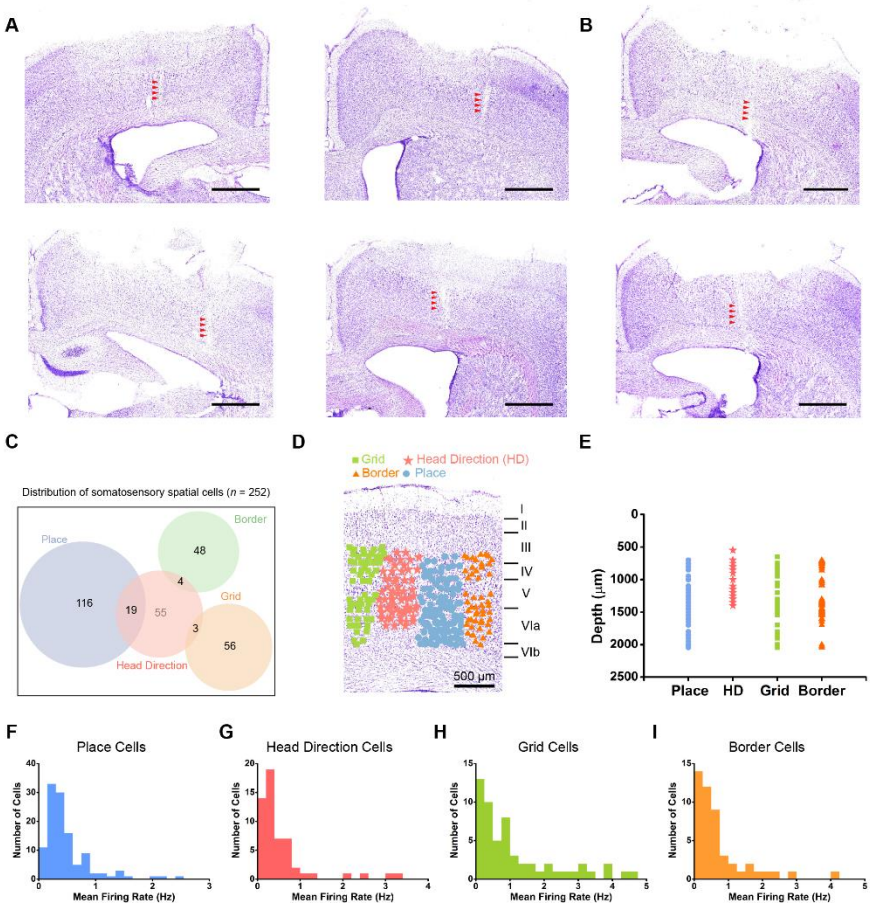


**Fig. S1 Recording locations and distributions of spatial cell types in the primary somatosensory cortex.**

(**A**) Nissl-stained coronal brain sections show electrode tracks (arrowheads) and final recording positions in four rats with tetrodes implanted in the primary somatosensory cortex. Scale bar, 1 mm. (**B**) Nissl-stained coronal brain sections showing representative recording locations (arrowheads) for two additional rats for whisker trimming experiment. Scale bar, 0.5 mm. (**C**) Venn diagram displaying the distribution of four different somatosensory spatial cell types. (**D**) The approximate laminar locations of recorded S1 spatial cells. Scale bar, 1 mm. (**E**) Distribution of recording locations within the S1 labelled with the same marker/color scheme as (**D**). (**F-I**) The distribution of mean firing rate of identified somatosensory place cells (**F**), head direction cells (**G**), border cells (**H**) and grid cells (**I**).

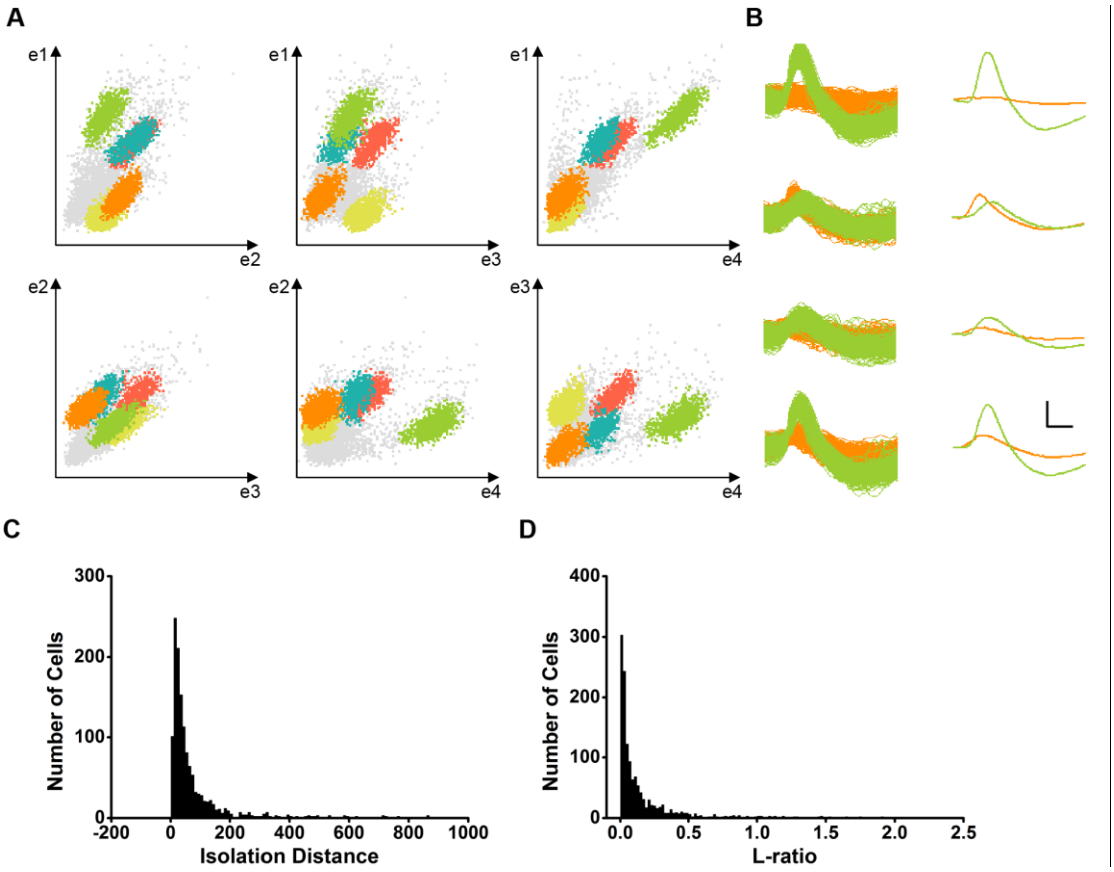


**Fig. S2 Cluster diagrams, waveforms and isolation quality of spike clusters recorded from the somatosensory cortex.**

(**A**) Scatterplots show the relationship between peak-to-trough amplitudes for all spikes for each wire (e1-e4) in a tetrode. (**B**) Overlaid and mean waveforms from two separated green and orange clusters in the scatterplots are shown for four electrodes from the same tetrode. Scale bar, 150 µV, 200 µs. (**C**) The distribution of isolation distance for identified S1 units. (**D**) Same as C for the L-ratio.

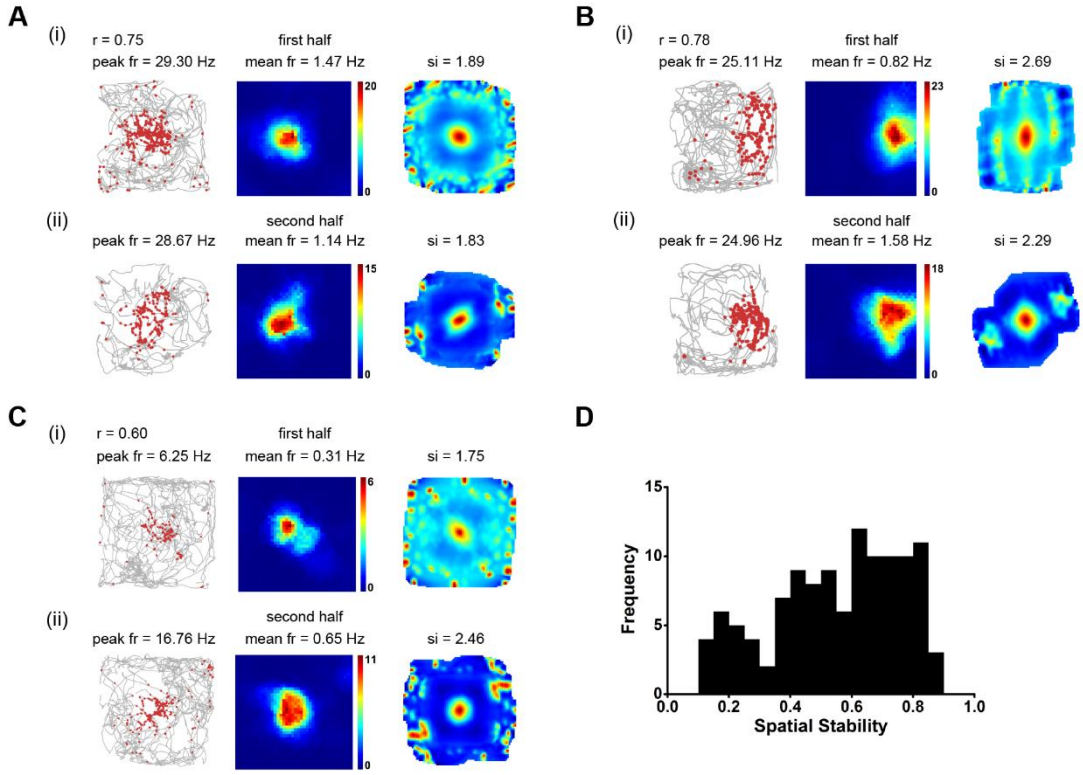


**Fig. S3 Spatial stability of somatosensory place cells.**

(**A-C**) Intra-trial spatial stability between the first and second halves of three representative place cells from **Fig. 1B**. Trajectory (grey line) with superimposed spike locations (red dots) (left column); rate maps (middle column) and autocorrelation maps (right column) for the first half (**i**) and the second half (**ii**) of the trials. Firing rate is color-coded with blue indicating minimum firing rate and red indicating maximum firing rate. The scale of the autocorrelation maps is twice that of the spatial firing rate maps. Peak firing rate (fr), mean firing rate (fr) and spatial information (si) are labelled at the top of the plots. Pearson's correlation coefficients of firing rate maps between the first and second halves are indicated with *r* at the top-left corner. (**D)** Distribution of spatial stability of firing rate maps between the first and second halves of all identified S1 place cells.

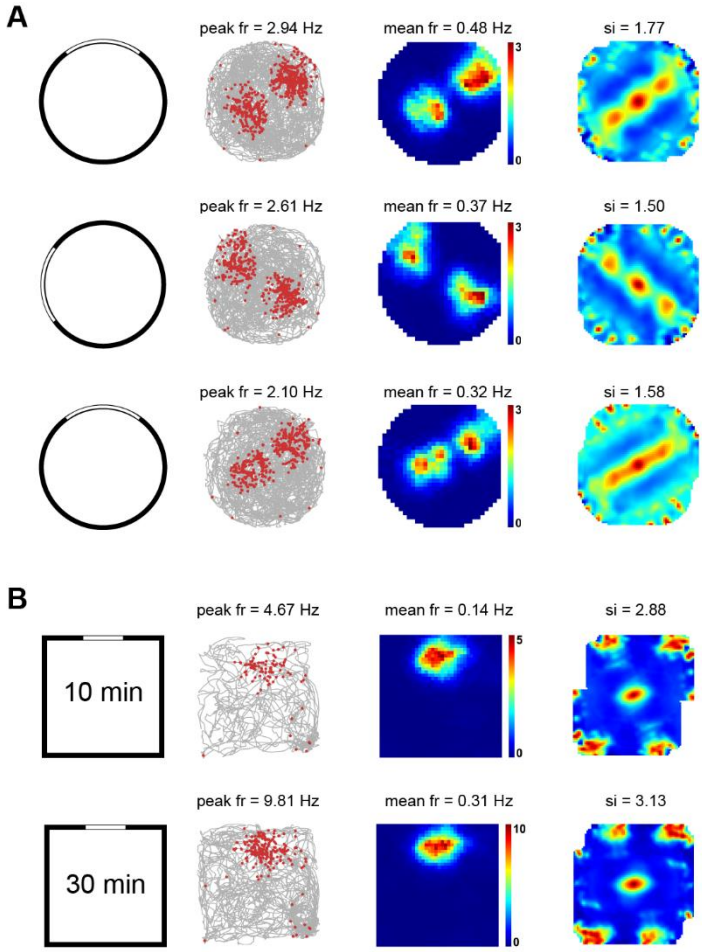


**Fig. S4 Cue-rotation control of somatosensory place cell signal and persistence of place fields from longer recording sessions.**

(**A**) Each panel shows the response of the same somatosensory place cell during three sessions of the cue-rotation condition. Top panels, before the cue-rotation; middle panels, counterclockwise 90° of cue-rotation; bottom panels, cue-rotation back to the original condition. The cue card is represented by a white arc in each panel. (**B**) Spatial stability of one representative somatosensory place cell between the short (top panels) and longer (bottom panels) recording sessions. Trajectory (grey line) with superimposed spike locations (red dots) (left middle column); spatial firing rate maps (middle right column) and autocorrelation diagrams (right column). Firing rate is color-coded with blue indicating minimum firing rate and red indicating maximum firing rate. The scale of the autocorrelation maps is twice that of the spatial firing rate maps. Peak firing rate (fr), mean firing rate (fr) and spatial information (si) for each recording sessions are labelled at the top of the panels.

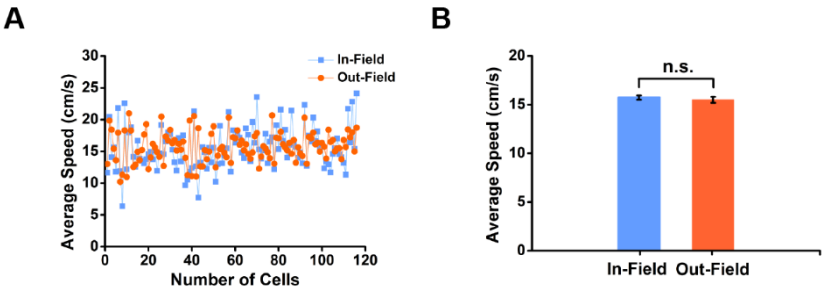


**Fig. S5 The distribution of the average in-field and out-field running speed for place cells in S1HL.**

(**A**) The distribution of the average running speed within and outside the firing fields of all identified place cells in S1HL. (**B**) The comparison of the average in-field and out-field running speed. $n$ = 116, $P$ = 0.36, two-tailed paired $t$-test, n.s., not significant.

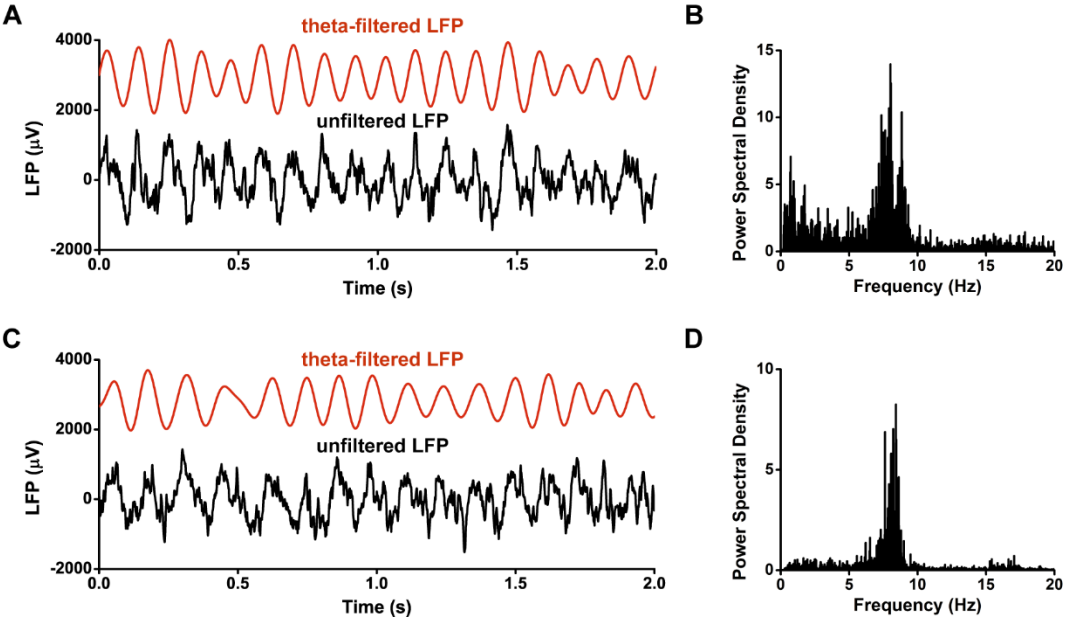


**Fig. S6 Theta oscillations of the local field potentials in the somatosensory cortex during locomotion.**

(**A** and **C**) Two representative traces of local field potentials during locomotion. Unfiltered signal is indicated in black and theta-filtered signal is indicated in red. The local field potentials exhibit persistent theta rhythmicity in the frequency range of 4-11 Hz. (**B** and **D**) Power spectral density plot of the recording sessions from **A** and **C**, respectively.

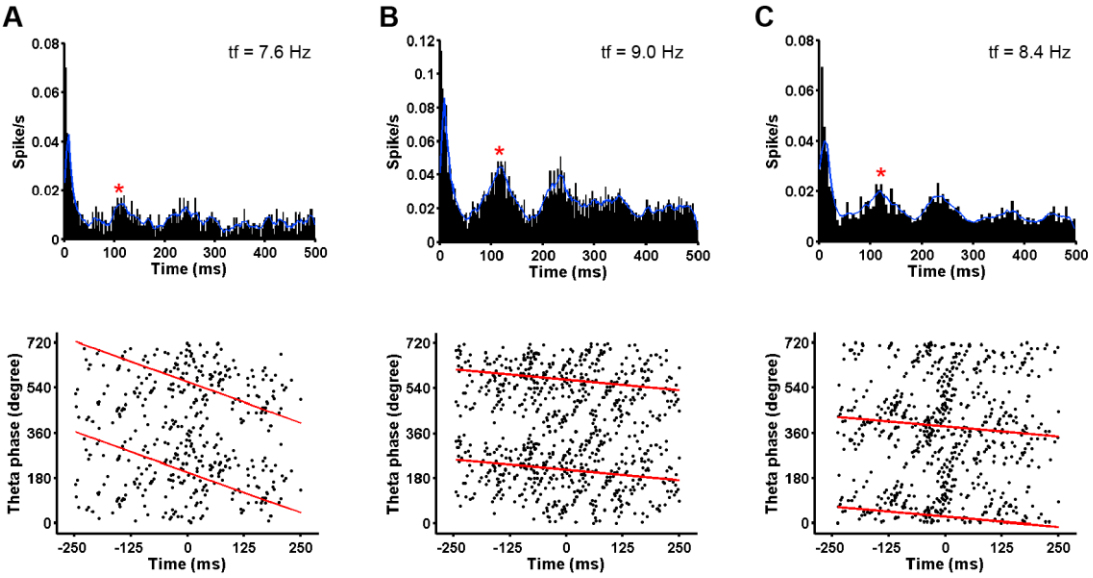


**Fig. S7 Theta-modulation and phase precession of somatosensory place cells.** (**A-C**) Top panels show spike time autocorrelation diagrams, with a red asterisk indicating the first peak in the recorded place cells identical to three representative somatosensory place cells in **Fig. 1B**. Peak theta frequency (tf) is labeled at the top of the panels. Bottom panels show the scatter plot of the local field potential theta phase versus spiking time corresponding to the same representative place cells in **Fig. 1B**, with the red line indicating the fitted slope of phase distribution within two theta cycles. Three somatosensory place cells all show significant theta precession (circular test, $P < 0.001$, 0.001 and 0.001, respectively).

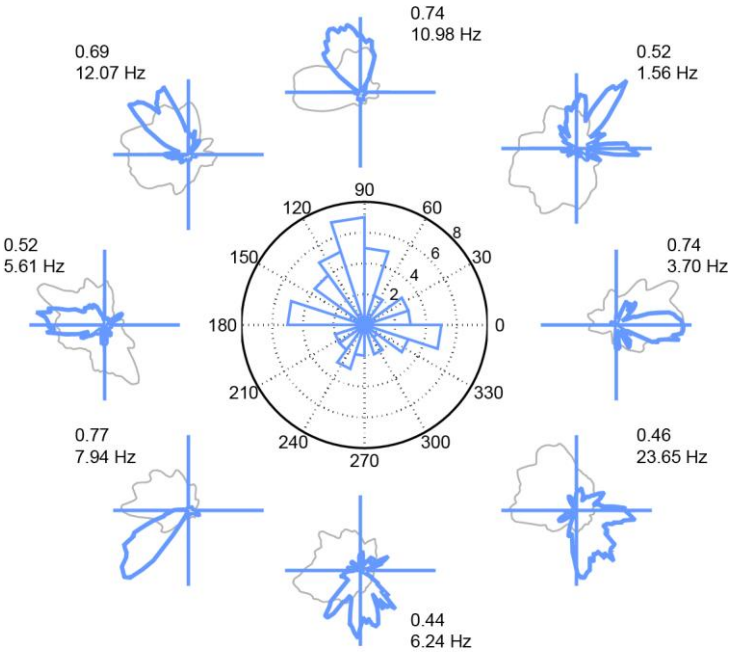


**Fig. S8 Preferred direction of recorded head direction cells from S1HL.**

The center polar plot shows the distribution of the peak firing direction of all identified somatosensory head direction cells. The preferred head direction exhibits a uniform distribution ($P$ = 0.60, Rayleigh's test). Variations in head direction tuning curves of eight representative S1 head direction cells are shown.

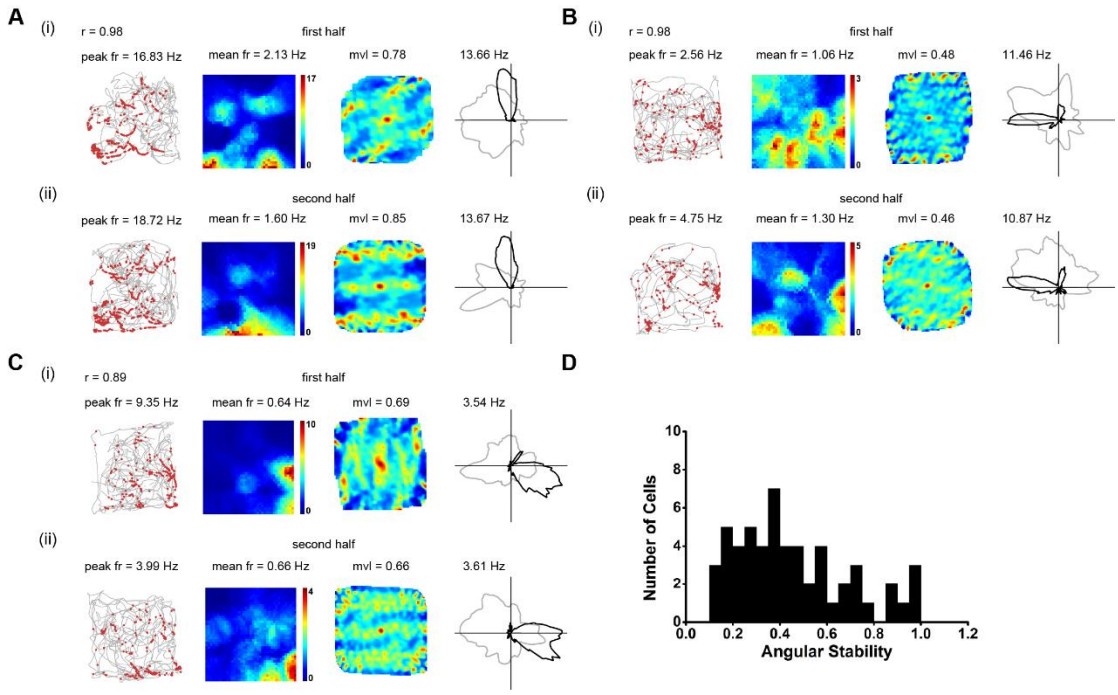


**Fig. S9 Angular stability of somatosensory head direction cells.**

(**A-C**) Intra-trial angular stability between the first and second halves of three representative head direction cells from **Fig. 2A**. Trajectory (grey line) with superimposed spike locations (red dots) (left column); spatial firing rate maps (middle left column), autocorrelation diagrams (middle right column) and head direction tuning curves (black) plotted against dwell-time polar plot (grey) (right column) for the first half (**i**) and second half (**ii**) of the trials. Firing rate is color-coded with blue indicating minimum firing rate and red indicating maximum firing rate. The scale of the autocorrelation maps is twice that of the spatial firing rate maps. Peak firing rate (fr), mean firing rate (fr), mean vector length (mvl) and angular peak rate for each representative head direction cell are labelled at the top of the panels. Correlation coefficients of the distributed firing rate across all directional bins between the first and second halves of individual recording trials are indicated with *r*. (**D)** Population histogram of angular stability of the distributed firing rate across all directional bins between the first and second halves of all identified S1 head direction cells.

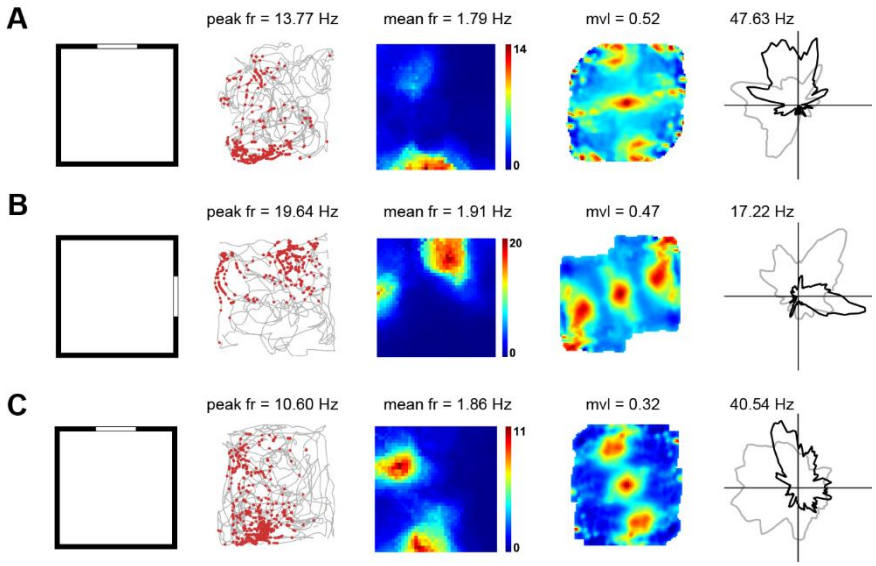


**Fig. S10 Cue-rotation control of somatosensory head directional responses.** (**A-C**) Each panel shows the response of the same S1 head direction cell during three recording trails during the cue-rotation condition. Top panels, before the cue-rotation (**A**); middle panels, clockwise 90° of cue-rotation (**B**); bottom panels, cue-rotation back to the original condition (**C**). The cue card is represented by a white line in each panel. The experimental diagram (left column); trajectory (grey line) with superimposed spike

locations (red dots) (middle left column); spatial firing rate maps (middle column), autocorrelation diagrams (middle right column) and head direction tuning curves (black) plotted against dwell-time polar plot (grey) (right column) for each recording trial. Firing rate is color-coded with blue indicating minimum firing rate and red indicating maximum firing rate. The scale of the autocorrelation maps is twice that of the spatial firing rate maps. Peak firing rate (fr), mean firing rate (fr), mean vector length (mvl) and angular peak rate for each representative head direction cell are labelled at the top of the panels.

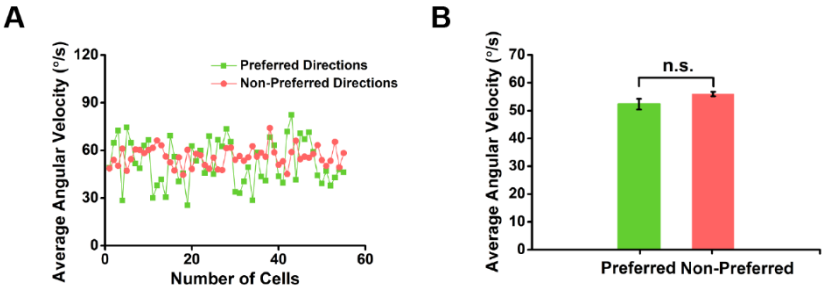


**Fig. S11 The distribution of the average angular velocity in the preferred and non-preferred firing directions for head direction cells in S1HL.**

(**A**) The distribution of the average angular velocity in the "preferred firing directions" and "non-preferred firing directions" for all identified head direction cells in S1HL. (**B**) The comparison of the angular velocity in the "preferred firing directions" and "non-preferred firing directions". $n = 55$, $P = 0.12$, two-tailed paired $t$-test, n.s., not significant.

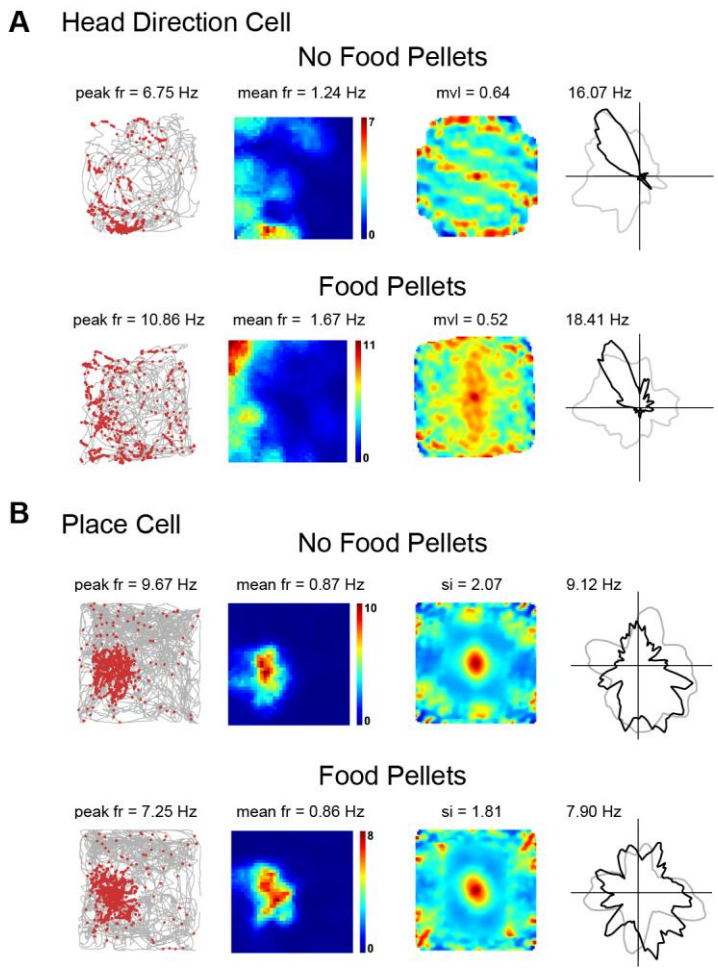


**Fig. S12 Somatosensory place and head direction cells in the presence or absence of food pellet.**

(**A**) The directional tuning of the same S1 head direction cell recorded with (top panels) and without (bottom panels) food pellets. (**B**) The firing fields of the same S1 place cell recorded with (top panels) and without (bottom panels) food pellets. Trajectory (grey line) with superimposed spike locations (red dots) (left column); spatial firing rate maps (middle left column), autocorrelation diagrams (middle right column) and head direction tuning curves (black) plotted against dwell-time polar plot (grey) (right column). Firing rate is color-coded with blue indicating minimum firing rate and red indicating maximum firing rate. The scale of the autocorrelation maps is twice that of the spatial firing rate maps. Peak firing rate (fr), mean firing rate (fr), mean vector length (mvl) or spatial information (si) and angular peak rate for each representative head direction cell are labelled at the top of the panels.

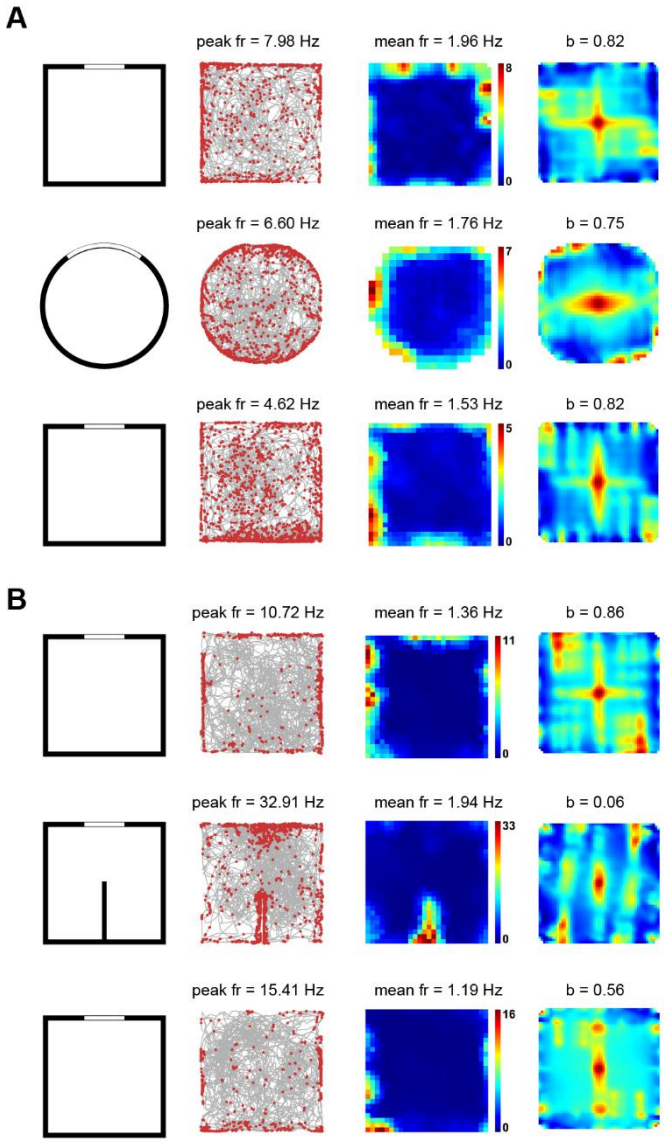


**Fig. S13 Preserved firing across different geometric shapes and spatial responses to the external inserts of somatosensory border cells.**

(**A**) A representative S1 border cell preserves the firing patterns in the square and cylindrical box. Top panels, original square running box; middle panels, cylindrical box; bottom panels, back to the original square box. (**B**) A representative S1 border cell recorded in the square enclosure with or without one external insert. Top panels, the square enclosure without insert; middle panels, the same square enclosure with an internal insert; bottom panels, the same square enclosure after removing the internal insert. The experimental diagram (left column); trajectory (grey line) with superimposed spike locations (red dots) (middle left column); rate maps (middle right column) and autocorrelation diagrams (right column) for each recording trail. Firing

rate is color-coded with blue indicating minimum firing rate and red indicating maximum firing rate. The scale of the autocorrelation maps is twice that of the spatial firing rate maps. Peak firing rate (fr), mean firing rate (fr) and border score (b) for each recording session are labelled at the top of the panels.

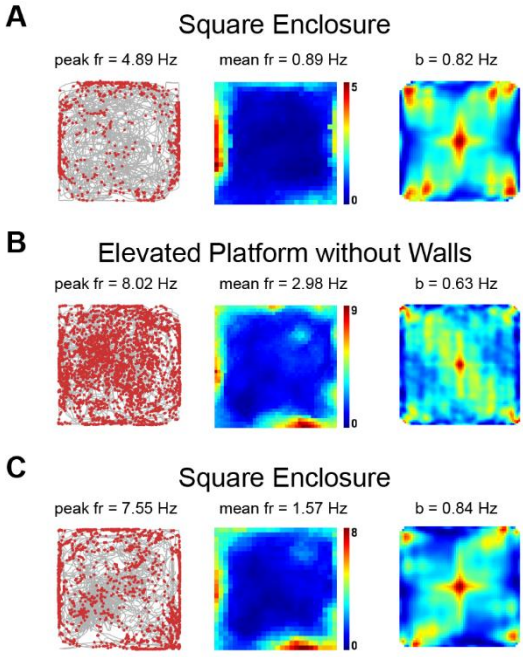


**Fig. S14 Somatosensory border cells recorded from the elevated platform without walls.**

(**A-C**) The firing fields of the same S1 border cell recorded in the square box (**A**), in the elevated platform without walls (**B**) and back to the square box (**C**). Trajectory (grey line) with superimposed spike locations (red dots) (left column); heat maps of firing rate (middle column) and autocorrelation maps (right column). Firing rate is color-coded with blue indicating minimum firing rate and red indicating maximum firing rate. The scale of the autocorrelation maps is twice that of the spatial firing rate maps. Peak firing rate (fr), mean firing rate (fr) and border score (b) for each representative border cell are labelled at the top of the panels.

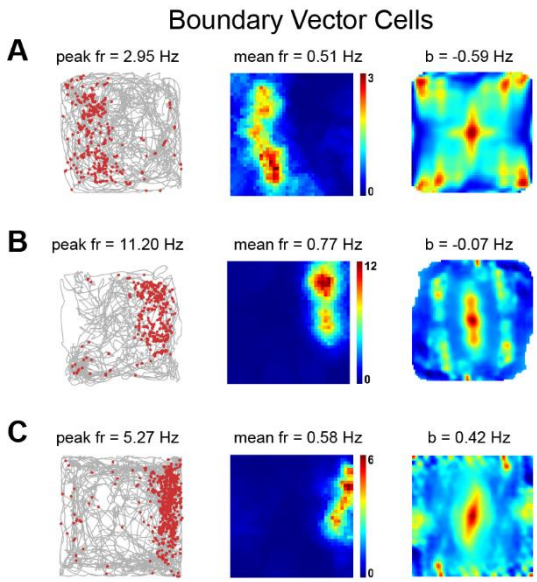


**Fig. S15 Boundary vector cells recorded from the S1HL.**

(**A-C**) Three representative examples of somatosensory boundary vector cells. Trajectory (grey line) with superimposed spike locations (red dots) (left column); heat maps of firing rate (middle column) and autocorrelation diagrams (right column). Firing rate is color-coded with blue indicating minimum firing rate and red indicating maximum firing rate. The scale of the autocorrelation maps is twice that of the spatial firing rate maps. Peak firing rate (fr), mean firing rate (fr) and border score (b) for each representative boundary vector cell are labelled at the top of the panels.

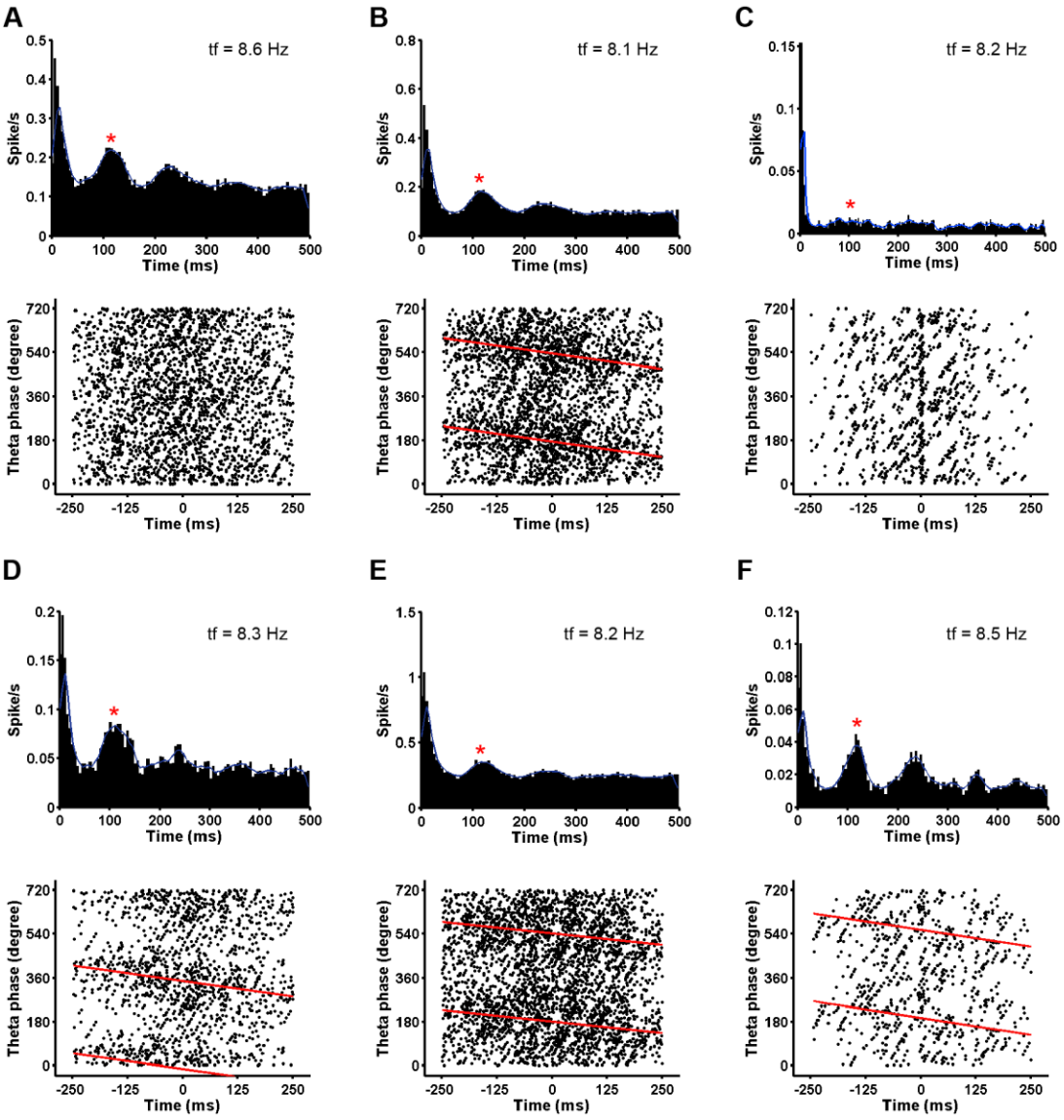


**Fig. S16 Theta modulation and phase precession of somatosensory regular and irregular grid cells.**

Panels **A**, **B** and **C** are regular grid cells corresponding to the same representative regular grid cells in **Fig. 4A**. Panels **D**, **E** and **F** are irregular grid cells corresponding to the same representative irregular grid cells in **Fig. 4G**. The top panels showed spike time autocorrelation diagrams, with a red asterisk indicating the first peak in the recorded grid cells identical to representative somatosensory regular and irregular grid cells in **Fig. 4**. Peak theta frequency (tf) was labeled at the top of the panels. The bottom panel showed the scatter plot of the local field potential theta phase versus spiking time of recorded somatosensory corresponding to the same representative grid cells in **Fig. 4**, with the red line indicating the fitted slope of phase distribution within two theta

cycles.

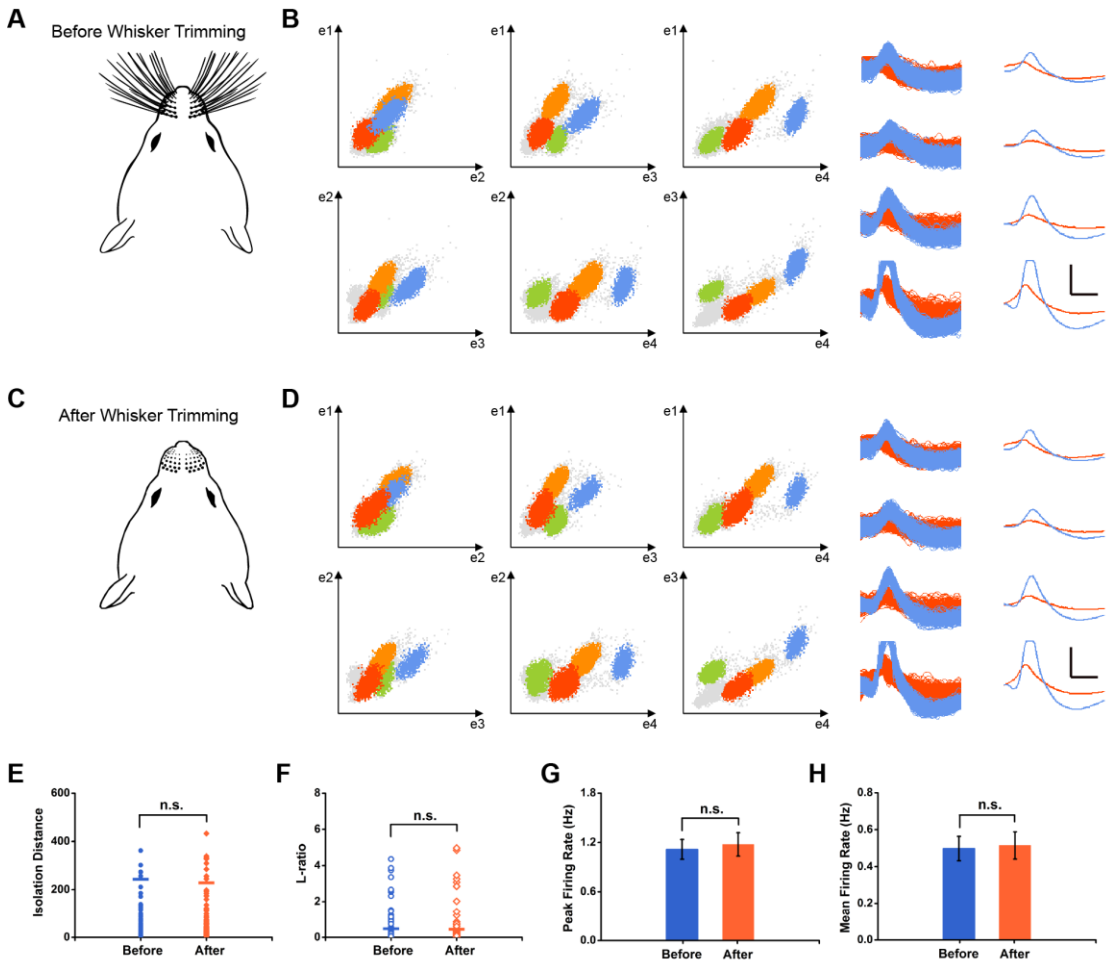


**Fig. S17 Preserved firing properties of the isolated somatosensory units before and after whisker trimming.**

(**A** and **C**) The diagram showing the rat before (**A**) and after (**C**) whisker trimming. (**B** and **D**) Scatterplots show preserved cluster diagrams before (**B**) and after (**D**) whisker trimming of the same tetrode from the same recording rat. Each individual dot represents a single recorded spike. Waveforms from two separated blue and red clusters in the scatterplots are shown for four electrodes from the same tetrode. The waveforms remain unchanged after whisker trimming. Scale bar, 150 μV, 300 μs. (**E**) The comparison of isolation distance for identified S1 units right before and after whisker trimming. (**F**) Same as **E** for the L-ratio. (**G**) Same as **F** for the mean firing rate. (**H**) Same as **G** for the peak firing rate. $n$ = 78, two-tailed paired $t$-test, n.s., not significant.

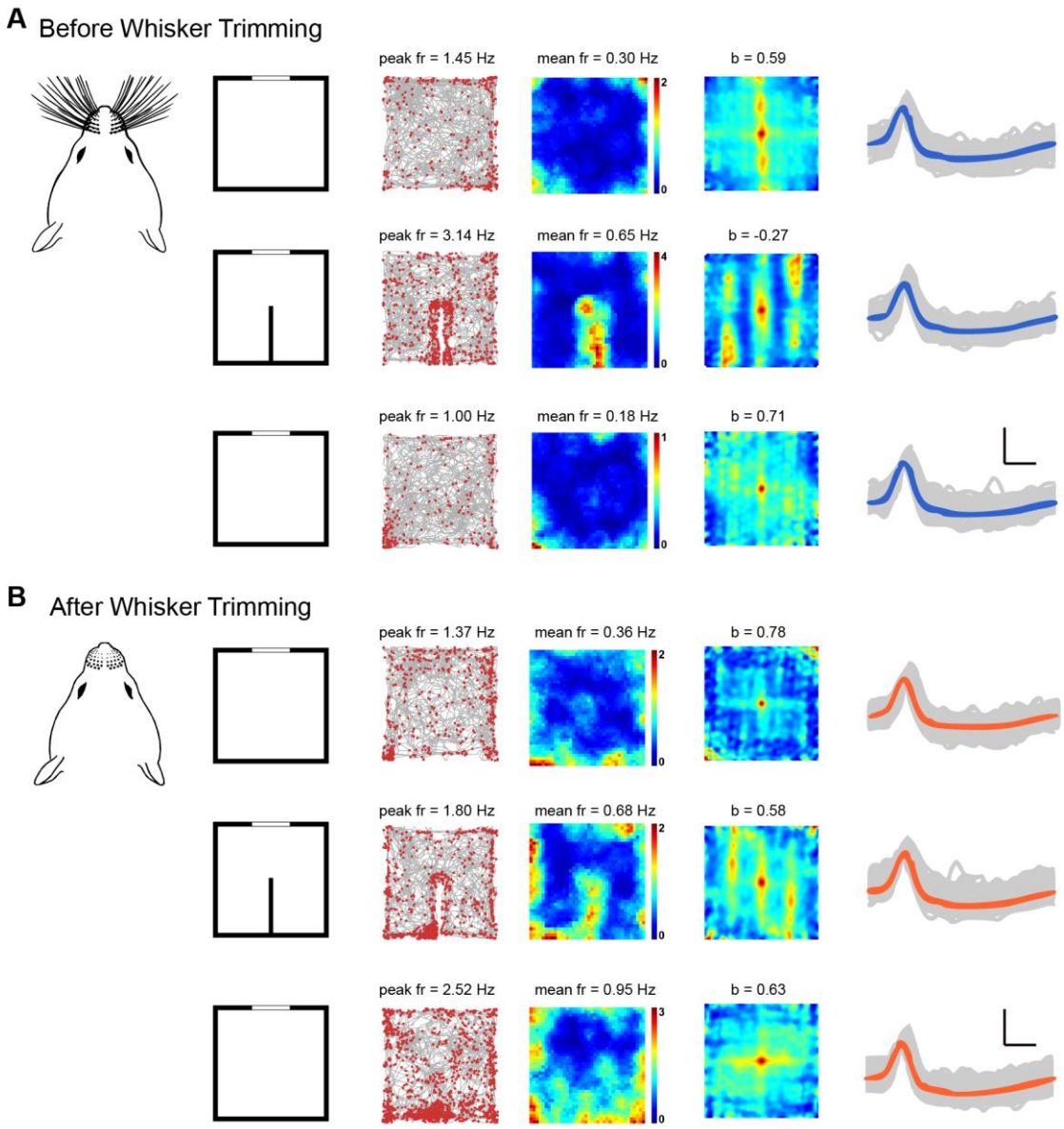


**Fig. S18 Preserved spatial firing properties of the same somatosensory border cell before and after whisker trimming.**

(**A** and **B**) The diagram showing the rat before (**A**) and after (**B**) whisker trimming. A representative somatosensory border cell preserves the firing patterns in the square box with (top and bottom panels) and without (middle panels) the internal insert before and after whisker trimming. The experimental diagram (left column); trajectory (grey line) with superimposed spike locations (red dots) (middle left column); rate maps (middle column), autocorrelation maps (middle right column) and waveform shapes (right column) for each recording trial from the same S1 border cell. Firing rate is color-coded with blue indicating minimum firing rate and red indicating maximum firing rate. The

scale of the autocorrelation maps is twice that of the spatial firing rate maps. Peak firing rate (fr), mean firing rate (fr) and border score (b) for each recording session are labelled at the top of the panels. Scale bar, 100 µV, 200 µs.

## References


1. Akers, R.M., and Killackey, H.P. (1978). Organization of corticocortical connections in the parietal cortex of the rat. J Comp Neurol *181*, 513-537.
2. Alexander, A.S., and Nitz, D.A. (2017). Spatially Periodic Activation Patterns of Retrosplenial Cortex Encode Route Sub-spaces and Distance Traveled. Current biology : CB *27*, 1551-1560 e1554.
3. Ashe, J., and Georgopoulos, A.P. (1994). Movement parameters and neural activity in motor cortex and area 5. Cerebral cortex (New York, NY : 1991) *4*, 590-600.
4. Bjerknes, T.L., Dagslott, N.C., Moser, E.I., and Moser, M.B. (2018). Path integration in place cells of developing rats. Proceedings of the National Academy of Sciences of the United States of America *115*, E1637-E1646.
5. Bjerknes, T.L., Langston, R.F., Kruge, I.U., Moser, E.I., and Moser, M.B. (2015). Coherence among head direction cells before eye opening in rat pups. Current biology : CB *25*, 103-108.
6. Bjerknes, T.L., Moser, E.I., and Moser, M.B. (2014). Representation of geometric borders in the developing rat. Neuron *82*, 71-78.
7. Boccara, C.N., Sargolini, F., Thoresen, V.H., Solstad, T., Witter, M.P., Moser, E.I., and Moser, M.B. (2010). Grid cells in pre- and parasubiculum. Nat Neurosci *13*, 987-994.
8. Bolding, K.A., Ferbinteanu, J., Fox, S.E., and Muller, R.U. (2019). Place cell firing cannot support navigation without intact septal circuits. Hippocampus.
9. Bonnevie, T., Dunn, B., Fyhn, M., Hafting, T., Derdikman, D., Kubie, J.L., Roudi, Y., Moser, E.I., and Moser, M.B. (2013). Grid cells require excitatory drive from the hippocampus. Nature neuroscience *16*, 309-317.
10. Brandon, M.P., Bogaard, A.R., Libby, C.P., Connerney, M.A., Gupta, K., and Hasselmo, M.E. (2011). Reduction of theta rhythm dissociates grid cell spatial periodicity from directional tuning. Science *332*, 595-599.
11. Brecht, M. (2017). The Body Model Theory of Somatosensory Cortex. Neuron *94*, 985-992.
12. Buetfering, C., Allen, K., and Monyer, H. (2014). Parvalbumin interneurons provide grid cell-driven recurrent inhibition in the medial entorhinal cortex. Nat Neurosci *17*, 710-718.
13. Buzsaki, G., and Moser, E.I. (2013). Memory, navigation and theta rhythm in the hippocampal-entorhinal system. Nat Neurosci *16*, 130-138.
14. Buzsaki, G., Stark, E., Berenyi, A., Khodagholy, D., Kipke, D.R., Yoon, E., and Wise, K.D. (2015). Tools for probing local circuits: high-density silicon probes combined with optogenetics. Neuron *86*, 92-105.

15. Cacucci, F., Lever, C., Wills, T.J., Burgess, N., and O'Keefe, J. (2004). Theta-modulated place-by-direction cells in the hippocampal formation in the rat. J Neurosci *24*, 8265-8277.
16. Cenquizca, L.A., and Swanson, L.W. (2007). Spatial organization of direct hippocampal field CA1 axonal projections to the rest of the cerebral cortex. Brain Res Rev.
17. Chorev, E., Preston-Ferrer, P., and Brecht, M. (2016). Representation of egomotion in rat's trident and E-row whisker cortices. Nature neuroscience *19*, 1367-1373.
18. Cullen, K.E., and Taube, J.S. (2017). Our sense of direction: progress, controversies and challenges. Nat Neurosci *20*, 1465-1473.
19. Feldman, D.E., and Brecht, M. (2005). Map plasticity in somatosensory cortex. Science *310*, 810-815.
20. Fiser, A., Mahringer, D., Oyibo, H.K., Petersen, A.V., Leinweber, M., and Keller, G.B. (2016). Experience-dependent spatial expectations in mouse visual cortex. Nat Neurosci *19*, 1658-1664.
21. Fu, Q.G., Flament, D., Coltz, J.D., and Ebner, T.J. (1995). Temporal encoding of movement kinematics in the discharge of primate primary motor and premotor neurons. J Neurophysiol *73*, 836-854.
22. Fyhn, M., Molden, S., Witter, M.P., Moser, E.I., and Moser, M.B. (2004). Spatial representation in the entorhinal cortex. Science *305*, 1258-1264.
23. Gaykema, R.P., Luiten, P.G., Nyakas, C., and Traber, J. (1990). Cortical projection patterns of the medial septum-diagonal band complex. J Comp Neurol *293*, 103-124.
24. Gener, T., Perez-Mendez, L., and Sanchez-Vives, M.V. (2013). Tactile modulation of hippocampal place fields. Hippocampus.
25. Georgopoulos, A.P., Caminiti, R., and Kalaska, J.F. (1984). Static spatial effects in motor cortex and area 5: quantitative relations in a two-dimensional space. Exp Brain Res *54*, 446-454.
26. Georgopoulos, A.P., Kalaska, J.F., Caminiti, R., and Massey, J.T. (1982). On the relations between the direction of two-dimensional arm movements and cell discharge in primate motor cortex. J Neurosci *2*, 1527-1537.
27. Goodridge, J.P., Dudchenko, P.A., Worboys, K.A., Golob, E.J., and Taube, J.S. (1998). Cue control and head direction cells. Behavioral neuroscience *112*, 749-761.
28. Hafting, T., Fyhn, M., Molden, S., Moser, M.B., and Moser, E.I. (2005). Microstructure of a spatial map in the entorhinal cortex. Nature *436*, 801-806.
29. Hales, J.B., Schlesiger, M.I., Leutgeb, J.K., Squire, L.R., Leutgeb, S., and Clark, R.E. (2014). Medial entorhinal cortex lesions only partially disrupt hippocampal place cells and hippocampus-dependent place memory. Cell reports *9*, 893-901.
30. Harris, K.D., Hirase, H., Leinekugel, X., Henze, D.A., and Buzsaki, G. (2001). Temporal interaction between single spikes and complex spike bursts in hippocampal pyramidal cells. Neuron *32*, 141-149.
31. Hok, V., Jacob, P.-Y., Bordiga, P., Truchet, B., Poucet, B., and Save, E. (2018). A

spatial code in the dorsal lateral geniculate nucleus. bioRxiv, 473520.
32. Insausti, R., Herrero, M.T., and Witter, M.P. (1997). Entorhinal cortex of the rat: cytoarchitectonic subdivisions and the origin and distribution of cortical efferents. Hippocampus *7*, 146-183.
33. Jankowski, M.M., and O'Mara, S.M. (2015). Dynamics of place, boundary and object encoding in rat anterior claustrum. Front Behav Neurosci *9*, 250.
34. Jezek, K., Henriksen, E.J., Treves, A., Moser, E.I., and Moser, M.B. (2011). Theta-paced flickering between place-cell maps in the hippocampus. Nature *478*, 246-249.
35. Ji, D., and Wilson, M.A. (2006). Coordinated memory replay in the visual cortex and hippocampus during sleep. Nature neuroscience.
36. Jung, M.W., Wiener, S.I., and McNaughton, B.L. (1994). Comparison of spatial firing characteristics of units in dorsal and ventral hippocampus of the rat. J Neurosci *14*, 7347-7356.
37. Kaas, J.H. (1983). What, if anything, is SI? Organization of first somatosensory area of cortex. Physiological Reviews *63*, 206-231.
38. Karadimas, S.K., Satkunendrarajah, K., Laliberte, A.M., Ringuette, D., Weisspapir, I., Li, L., Gosgnach, S., and Fehlings, M.G. (2019). Sensory cortical control of movement. Nature neuroscience.
39. Kettner, R.E., Schwartz, A.B., and Georgopoulos, A.P. (1988). Primate motor cortex and free arm movements to visual targets in three-dimensional space. III. Positional gradients and population coding of movement direction from various movement origins. J Neurosci *8*, 2938-2947.
40. Khazipov, R., Sirota, A., Leinekugel, X., Holmes, G.L., Ben-Ari, Y., and Buzsaki, G. (2004). Early motor activity drives spindle bursts in the developing somatosensory cortex. Nature *432*, 758-761.
41. Killackey, H.P., and Sherman, S.M. (2003). Corticothalamic projections from the rat primary somatosensory cortex. J Neurosci *23*, 7381-7384.
42. Kjelstrup, K.B., Solstad, T., Brun, V.H., Hafting, T., Leutgeb, S., Witter, M.P., Moser, E.I., and Moser, M.B. (2008). Finite scale of spatial representation in the hippocampus. Science *321*, 140-143.
43. Koenig, J., Linder, A.N., Leutgeb, J.K., and Leutgeb, S. (2011). The spatial periodicity of grid cells is not sustained during reduced theta oscillations. Science *332*, 592-595.
44. Langston, R.F., Ainge, J.A., Couey, J.J., Canto, C.B., Bjerknes, T.L., Witter, M.P., Moser, E.I., and Moser, M.B. (2010). Development of the spatial representation system in the rat. Science *328*, 1576-1580.
45. Larkum, M. (2013). A cellular mechanism for cortical associations: an organizing principle for the cerebral cortex. Trends in neurosciences *36*, 141-151.
46. Lefort, S., Tomm, C., Floyd Sarria, J.C., and Petersen, C.C. (2009). The excitatory neuronal network of the C2 barrel column in mouse primary somatosensory cortex. Neuron *61*, 301-316.
47. Leutgeb, S., and Mizumori, S.J. (2002). Context-specific spatial representations

by lateral septal cells. Neuroscience *112*, 655-663.
48. Lever, C., Burton, S., Jeewajee, A., O'Keefe, J., and Burgess, N. (2009). Boundary vector cells in the subiculum of the hippocampal formation. J Neurosci *29*, 9771-9777.
49. Long, X., and Zhang, S.J. (2018). A novel somatosensory spatial navigation system outside the hippocampal formation. bioRxiv *doi: 10.1101/473090*.
50. Mathis, A., Mamidanna, P., Cury, K.M., Abe, T., Murthy, V.N., Mathis, M.W., and Bethge, M. (2018). DeepLabCut: markerless pose estimation of user-defined body parts with deep learning. Nature neuroscience *21*, 1281-1289.
51. McNaughton, B.L., Barnes, C.A., and O'Keefe, J. (1983). The contributions of position, direction, and velocity to single unit activity in the hippocampus of freely-moving rats. Exp Brain Res *52*, 41-49.
52. McNaughton, B.L., Battaglia, F.P., Jensen, O., Moser, E.I., and Moser, M.B. (2006). Path integration and the neural basis of the 'cognitive map'. Nat Rev Neurosci *7*, 663-678.
53. Moran, D.W., and Schwartz, A.B. (1999). Motor cortical representation of speed and direction during reaching. J Neurophysiol *82*, 2676-2692.
54. Moser, E.I., Kropff, E., and Moser, M.B. (2008). Place cells, grid cells, and the brain's spatial representation system. Annu Rev Neurosci *31*, 69-89.
55. Moser, E.I., Moser, M.B., and McNaughton, B.L. (2017). Spatial representation in the hippocampal formation: a history. Nat Neurosci *20*, 1448-1464.
56. Muller, R.U., and Kubie, J.L. (1987). The effects of changes in the environment on the spatial firing of hippocampal complex-spike cells. J Neurosci *7*, 1951-1968.
57. O'Keefe, J., and Conway, D.H. (1978). Hippocampal place units in the freely moving rat: why they fire where they fire. Exp Brain Res *31*, 573-590.
58. O'Keefe, J., and Dostrovsky, J. (1971). The hippocampus as a spatial map. Preliminary evidence from unit activity in the freely-moving rat. Brain Res *34*, 171-175.
59. O'Keefe, J., and Recce, M.L. (1993). Phase relationship between hippocampal place units and the EEG theta rhythm. Hippocampus *3*, 317-330.
60. Paninski, L., Fellows, M.R., Hatsopoulos, N.G., and Donoghue, J.P. (2004). Spatiotemporal tuning of motor cortical neurons for hand position and velocity. J Neurophysiol *91*, 515-532.
61. Paxinos, G., and Watson, C. (2007). The rat brain in stereotaxic coordinates, Vol 552 (Amsterdam: Elsevier).
62. Petersen, C.C.H. (2019). Sensorimotor processing in the rodent barrel cortex. Nat Rev Neurosci *20*, 533-546.
63. Poucet, B., Chaillan, F., Truchet, B., Save, E., Sargolini, F., and Hok, V. (2015). Is there a pilot in the brain? Contribution of the self-positioning system to spatial navigation. Front Behav Neurosci *9*, 292.
64. Quirk, G.J., Muller, R.U., and Kubie, J.L. (1990). The firing of hippocampal place cells in the dark depends on the rat's recent experience. J Neurosci *10*, 2008-2017.

65. Ranck, J.B. (1985). Head direction cells in the deep cell layer of dorsal presubiculum in freely moving rats. In Electrical Activity Of The Archicortex, G. Buzsaki, and C.H. Vanderwolf, eds. (Budapest: Akademiai Kiado), pp. 217–220.
66. Rancz, E.A., Moya, J., Drawitsch, F., Brichta, A.M., Canals, S., and Margrie, T.W. (2015). Widespread vestibular activation of the rodent cortex. J Neurosci *35*, 5926-5934.
67. Ravassard, P., Kees, A., Willers, B., Ho, D., Aharoni, D.A., Cushman, J., Aghajan, Z.M., and Mehta, M.R. (2013). Multisensory control of hippocampal spatiotemporal selectivity. Science *340*, 1342-1346.
68. Ray, S., Naumann, R., Burgalossi, A., Tang, Q., Schmidt, H., and Brecht, M. (2014). Grid-layout and theta-modulation of layer 2 pyramidal neurons in medial entorhinal cortex. Science *343*, 891-896.
69. Rich, P.D., Liaw, H.P., and Lee, A.K. (2014). Place cells. Large environments reveal the statistical structure governing hippocampal representations. Science *345*, 814-817.
70. Rubin, A., Yartsev, M.M., and Ulanovsky, N. (2014). Encoding of head direction by hippocampal place cells in bats. J Neurosci *34*, 1067-1080.
71. Sargolini, F., Fyhn, M., Hafting, T., McNaughton, B.L., Witter, M.P., Moser, M.B., and Moser, E.I. (2006). Conjunctive representation of position, direction, and velocity in entorhinal cortex. Science *312*, 758-762.
72. Schmitzer-Torbert, N., and Redish, A.D. (2004). Neuronal activity in the rodent dorsal striatum in sequential navigation: separation of spatial and reward responses on the multiple T task. J Neurophysiol *91*, 2259-2272.
73. Schubert, D., Staiger, J.F., Cho, N., Kotter, R., Zilles, K., and Luhmann, H.J. (2001). Layer-specific intracolumnar and transcolumnar functional connectivity of layer V pyramidal cells in rat barrel cortex. J Neurosci *21*, 3580-3592.
74. Sieben, K., Roder, B., and Hanganu-Opatz, I.L. (2013). Oscillatory entrainment of primary somatosensory cortex encodes visual control of tactile processing. J Neurosci *33*, 5736-5749.
75. Skaggs, W.E., McNaughton, B.L., Wilson, M.A., and Barnes, C.A. (1996). Theta phase precession in hippocampal neuronal populations and the compression of temporal sequences. Hippocampus *6*, 149-172.
76. Sofroniew, N.J., and Svoboda, K. (2015). Whisking. Curr Biol *25*, R137-140.
77. Solstad, T., Boccara, C.N., Kropff, E., Moser, M.B., and Moser, E.I. (2008). Representation of geometric borders in the entorhinal cortex. Science *322*, 1865-1868.
78. Stark, E., Drori, R., and Abeles, M. (2009). Motor cortical activity related to movement kinematics exhibits local spatial organization. Cortex; a journal devoted to the study of the nervous system and behavior *45*, 418-431.
79. Taube, J.S. (1995). Head direction cells recorded in the anterior thalamic nuclei of freely moving rats. J Neurosci *15*, 70-86.
80. Taube, J.S., Muller, R.U., and Ranck, J.B., Jr. (1990). Head-direction cells recorded from the postsubiculum in freely moving rats. I. Description and

quantitative analysis. J Neurosci *10*, 420-435.
81. Town, S.M., Brimijoin, W.O., and Bizley, J.K. (2017). Egocentric and allocentric representations in auditory cortex. PLoS Biol *15*, e2001878.
82. Tseng, P.H., Rajangam, S., Lehew, G., Lebedev, M.A., and Nicolelis, M.A.L. (2018). Interbrain cortical synchronization encodes multiple aspects of social interactions in monkey pairs. Sci Rep *8*, 4699.
83. Tukker, J.J., Tang, Q., Burgalossi, A., and Brecht, M. (2015). Head-Directional Tuning and Theta Modulation of Anatomically Identified Neurons in the Presubiculum. J Neurosci *35*, 15391-15395.
84. Umeda, T., Isa, T., and Nishimura, Y. (2019). The somatosensory cortex receives information about motor output. Science advances *5*, eaaw5388.
85. Welker, C., and Sinha, M.M. (1972). Somatotopic organization of SmII cerebral neocortex in albino rat. Brain research *37*, 132-136.
86. Welker, E., Hoogland, P.V., and Van der Loos, H. (1988). Organization of feedback and feedforward projections of the barrel cortex: a PHA-L study in the mouse. Exp Brain Res *73*, 411-435.
87. Wilber, A.A., Clark, B.J., Forster, T.C., Tatsuno, M., and McNaughton, B.L. (2014). Interaction of egocentric and world-centered reference frames in the rat posterior parietal cortex. J Neurosci *34*, 5431-5446.
88. Wills, T.J., Cacucci, F., Burgess, N., and O'Keefe, J. (2010). Development of the hippocampal cognitive map in preweanling rats. Science *328*, 1573-1576.
89. Wilson, M.A., and McNaughton, B.L. (1993). Dynamics of the hippocampal ensemble code for space. Science *261*, 1055-1058.
90. Yamawaki, N., and Shepherd, G.M. (2015). Synaptic circuit organization of motor corticothalamic neurons. J Neurosci *35*, 2293-2307.
91. Yartsev, M.M., Witter, M.P., and Ulanovsky, N. (2011). Grid cells without theta oscillations in the entorhinal cortex of bats. Nature *479*, 103-107.
92. Yin, A., Tseng, P.H., Rajangam, S., Lebedev, M.A., and Nicolelis, M.A.L. (2018). Place Cell-Like Activity in the Primary Sensorimotor and Premotor Cortex During Monkey Whole-Body Navigation. Sci Rep *8*, 9184.
93. Zhang, S., and Manahan-Vaughan, D. (2013). Spatial Olfactory Learning Contributes to Place Field Formation in the Hippocampus. Cerebral cortex (New York, NY : 1991).
94. Zhang, S.J., Ye, J., Miao, C., Tsao, A., Cerniauskas, I., Ledergerber, D., Moser, M.B., and Moser, E.I. (2013). Optogenetic dissection of entorhinal-hippocampal functional connectivity. Science *340*, 1232627.